Empirical Evidence of Frequency-Dependent Directivity Effects from Small-to-Moderate Normal Fault Earthquakes in Central Italy

Leonardo Colavitti[1], Giovanni Lanzano[1], Sara Sgobba[1], Francesca Pacor[1], František Gallovič[2]

[1] National Institute of Geophysics and Volcanology, Section of Seismology applied to Engineering, Milano, Italy

[2] Charles University, Faculty of Mathematics and Physics, Department of Geophysics, Prague, Czech Republic

Corresponding author: Leonardo Colavitti (leonardo.colavitti@ingv.it)

Key Points:

- Statistical procedure to detect directivity effects in small-to-moderate earthquakes analyzing the aleatory residuals of the ground motion
- The directive events are the 36% of the dataset and the distribution of rupture direction is aligned with the strikes of the faults system
- The observed directivity is a frequency-dependent band-limited phenomenon, which can occur up to 5 times the value of corner frequency

Abstract. Rupture directivity and its potential frequency dependence is an open issue within the seismological community, especially for small-to-moderate events. Here we provide a statistical overview based on empirical evidence of seismological observations, thanks to the large amount of high-quality seismic recordings (more than 30,000 waveforms) from Central Italy, which represents an excellent and almost unique natural laboratory of normal faulting earthquakes in the magnitude range between 3.4 and 6.5 within the time frame 2008-2018. In order to detect an anisotropic distribution of ground motion amplitudes due to the rupture directivity, we fit the smoothed Fourier Amplitude Spectra (FAS) cleared of source-, site- and path- effects. According to our criteria, about 36% of the analyzed events (162 out of 456) are directive and the distribution of rupture direction is aligned with the strikes of the major faults of the Central Apennines. We find that the directivity is a band-limited phenomenon whose width may extend up to 5 times the corner frequency. The results of this research provide useful insights to parameterize directivity, to be explicitly implemented in future ground motion modeling and scenario predictions.

Plain Language Summary. In seismology, directivity is one of the source phenomena that causes large spatial variability of earthquake ground motions and is related to the features of the rupture propagation along the fault. The importance of this effect is very well known for large-magnitude events (M > 6), while it is still an open issue for small-to-moderate events. The aim of this paper is to recognize directive events and quantify their strength in Central Italy, using a large dataset of earthquakes in the magnitude range 3.4-6.5 that occurred between 2008 and 2018. We find that about 36% of the analyzed events are directive, caused by rupture propagations oriented along the NW-SE alignment of the Central Apennines fault systems. Furthermore, we find that directivity is a band-limited phenomenon and that as the directivity gets stronger, the frequency band becomes wider. Our contribution provides a useful insight with the possibility to improve the parametrization of directivity within the empirical seismic hazard assessment.

1 Introduction

Directivity effect of an earthquake is the focusing of the radiated seismic wave energy due to the rupture propagation along the fault (Ben-Menahem, 1961; Joyner, 1991; Anderson, 2007; Boatwright, 2007). Earthquake directivity represents the analogue of the Doppler effect for sound and light waves (Douglas et al., 1988; Pacor et al., 2016a), which shifts the frequency of a moving oscillator to higher frequency when the oscillator moves toward an observer, and lower frequency when it moves away.

This phenomenon, which represents one of the key factors in featuring the spatial distribution of the seismic shaking, produces azimuthal and spectral variations in the ground motion, that can be used to infer information on both the orientation of the fault plane and on the modes of rupture propagation (Abercrombie et al., 2017). Furthermore, the quantification of the directivity-induced amplifications has important consequences in seismic hazard assessment, in terms of ground-motion amplitude and associated variability (Spagnuolo et al., 2012; Chioccarelli and Iervolino, 2014). Although the importance of directivity is widely recognized for both seismological studies on earthquake sources and engineering applications, a clear picture of how strongly and how often it occurs is not yet available.

In the 90s, the directivity phenomenon was initially observed and modeled for large events, such as the two recordings of the 1992 Mw 7.3 Landers earthquake at Lucerne and Joshua Tree stations (Velasco et al., 1994; Bernard et al., 1996; Pacor et al., 2005) or the 1994 Mw 6.7 Northridge earthquake (Dreger, 1994; Abrahamson and Somerville, 1996; Somerville et al., 1996), since earthquake directivity was combined with the effects of the finite size of the fault. Over the years, with the development of the broad-band seismic networks, the data quantity and quality have improved considerably. For this reason, nowadays we are able to observe directivity even for moderate-sized (McGuire, 2004; Boatwright, 2007; Seekins and Boatwright, 2010; Tan et al., 2010; López-Comino et al., 2012; Courboulex et al., 2013; Calderoni et al., 2015; Wen et al., 2015; Convertito et al., 2016; Pacor et al., 2016a) and small earthquakes (Yamada et al., 2005; Tomic et al., 2009; Chen et al., 2010). Directivity in small earthquakes is not a sporadic phenomenon, and recent studies of large datasets in California (Ross et al., 2020) and Japan (Yoshida, 2019) have shown that asymmetric ruptures (unilateral) seem predominant with respect to symmetric ones (bilateral), occurring in more than 60% of the cases analyzed.

One of the most common techniques to capture directivity effects of smaller earthquakes is to measure the duration of the source pulse (called Apparent Source Time Function) at each site and then model it by a line source (e.g. Tomic et al., 2009; Folesky et al., 2016 among the others). Trugman (2022) has recently proposed an innovative Bayesian technique to isolate source spectra using a generalized spectral decomposition inversion and applied it to magnitude M5 in the Southern California to infer some source properties, including directivity effects.

Much more debated is the question of a prevailing direction of rupture propagation in a given region or during a seismic sequence. On this aspect, the results are controversial, as are the physical causes that might determine a preferred direction. For instance, for the case of the 2012 Emilia seismic sequence in Italy, Convertito et al. (2013) observed that a variation of permeability might encourage the fracture in a preferred direction as a consequence of a local increase of the pore pressure and fluid flow rates: in this context, the source directivity can also enhance changes in permeability (López-Comino et al., 2021).

The effects of directivity on ground motion are magnitude and frequency dependent (Bernard et al., 1996). At low frequencies and for moderate-to-strong events, directivity can be responsible for coherent, potentially very destructive pulses with large amplitudes, while at high frequencies and for small-to-moderate events, the most evident effect is given by the shift of the corner frequencies that can result in high-frequency energy arrivals in short time intervals (Anderson, 2007). Modeling of the 2014 Mw 6 Napa earthquake by Gallovič (2016) suggested a preference of model with weak or no directivity effect at high frequencies to correctly explain the azimuthal variations of the strong ground motions. Based on empirical observations from seismic recordings, Pacor et al. (2016a) showed that high-frequency directivity can weaken due to source complexity even for small events.

In the context of empirical ground motion models (GMMs), directivity was clearly seen in the residuals of most earthquakes collected worldwide, such as in NGA-West (Rowshandel, 2010) or other recent near-source databases (Pacor et al., 2018; Sgobba et al., 2021b). Many researchers in the past have empirically modeled directivity effects by fitting the azimuthal variation of within-event residuals to get unbiased prediction (Somerville et al., 1997; Shahi and Baker, 2011; Sgobba et al., 2021c).

With the increasing dissemination of non-ergodic approaches for ground-motion modeling in highly sampled areas (e.g. Baltay et al., 2017; Kuehn et al., 2019; Lavrentiadis et al., 2021; Sgobba et al., 2021), thanks to the use of repeated observations, it is now possible to decompose further the residuals into systematic effects, also known as random-terms, via a mixed-effect regression approach (Stafford, 2014), permitting better isolation of different sources of the model variability. Yet, in non-ergodic models, directivity rupture effects are not repeatable in the sense that directivity from any earthquake does not allow predicting that of another event (Sahakian et al., 2019). Hence the directivity effect cannot be systematically quantified and removed from the total variability of the ground shaking as random-terms, but it can be found in the leftover regression residuals (i.e. as the remaining record-to-record variability of observed ground motion from model predictions).

Therefore, the frequency dependence of the directivity effects in seismic recordings can be inferred by analyzing the azimuthal and frequency dependence of these residuals terms corrected for systematic contributions related to the source and the sites (e.g. Ameri et al., 2009; Ren et al., 2017) and, in a fully non-ergodic approach, also to the path (Sgobba et al., 2021a). Recently, this approach was adopted to recognize directivity effects during some events of the 2016-2017 Central Italy seismic sequence (Calderoni et al., 2015; Calderoni et al., 2017; Ren et al., 2017; Luzi et al., 2017; Wang et al., 2019), revealing significant rupture-propagation complexity, both for small and moderate earthquakes.

In light of the above, it is clear that the literature studies on directivity modeling are mainly carried out with the aim of interpreting the spatial patterns of specific recorded seismic sequences or in order to find seismological features on simulated data. However, there is a lack of knowledge about the main statistical features related to directivity effects on a more extended dataset covering diverse earthquake scenarios and wide frequency intervals, gaining insights to empirically model ground shaking and to provide more physical constraints to their final predictions. Our work thus aims to increase this knowledge by recognizing the statistical features of directivity on the basis of a very dense dataset of records in Central Italy, which represents an almost unique natural laboratory for earthquakes occurring on normal faults (Boncio et al., 2000; Di Luccio et al., 2010; Bonini et al., 2016).

With this aim, we analyze the empirical frequency and azimuthal dependence of directivity imprinted in the distribution of the residuals between the observed and predicted data. In this work, we calibrate a fully non-ergodic GMM, in terms of Fourier Amplitude Spectra (FAS). The relaxation of the ergodic assumption represents a relevant step towards the empirical modeling of directivity, as it allows to remove all the systematic components of variability, related not only to the event and site, but also to the source-to-site path and source region. Indeed, 60-70% of the aleatory variance of the ground motion predictions can be associated with systematic effects (Abrahamson et al., 2019). The non-ergodic technique thus leads to better isolating the directivity contribution in the random term of the remaining residuals. The approach is entirely based on empirical observations, thanks to the large amounts of high-quality seismic recordings following the two main seismic sequences of L'Aquila in 2009 (Chiarabba et al., 2009; Walters et al., 2009) and Amatrice-Norcia in 2016 and 2017 (Chiaraluce et al., 2017; Pizzi et al., 2017).

The paper is outlined as follows: firstly, the dataset and the ground motion model used for the analysis are introduced, then directivity effects are modeled through an empirical approach based on residual decomposition, and the results are statistically analyzed. Finally, the main parameters controlling the phenomenon are identified for their potential implementation within ground motion predictive models in the field of engineering seismology such as for shaking scenarios and hazard assessments.

2 Dataset

The dataset is the same as used by Sgobba et al. (2021a) and consists of high-quality accelerometric and velocimetric waveforms related to stations and earthquakes located in Central Italy since 2008. The tectonic setting of this region is complex in terms of mechanical discontinuities and rheological properties (Carafa and Barba, 2011; Chiarabba et al., 2018), featuring mainly normal faults that caused several seismic sequences in the last 20 years (i.e. 1997-1998, Umbria-Marche Mw 6.0; 2009, L'Aquila Mw 6.1; 2016-2017, Amatrice-Visso-Norcia Mw 6.5; 2018, Muccia Mw 4.6). In order to guarantee more stable and robust analyses, we additionally set a threshold to at least 10 recordings for each station, according to the approach performed by Lanzano et al. (2017).

Fig. 1a shows the high density of events and stations in the study region, featuring a dense azimuthal sampling of source-to-site ray paths. The overall dataset analyzed in this study consists of more than 30,000 waveforms of 456 earthquakes in the magnitude range between 3.2 and 6.5, and 460 stations within 120 km from the epicenter, as demonstrated by the histograms in **Fig. 1b**. The recordings' distribution is strongly characterized by low magnitudes (panel on the right of **Fig. 1b**), with the most frequent value equal to 3.5 and with 70% of the recordings having a magnitude below 4. More than 80% of the bulk data is included in the distance range between 20 and 120 km (top panel on **Fig. 1b**).

Starting from this dataset, the study is conducted on the Fourier spectra smoothed using the Konno and Ohmachi (1998) algorithm (fixing the smoothing parameter b to 40) of the signal containing the S-phases. For each record, we use a distance-dependent energy criterion to identify S-wave time window (Pacor et al., 2016b). As time windows of records close to the epicenter could be very short (generally less than 2 s), we fix a minimum length of 4 s in order to guarantee an acceptable spectral resolution above 1 Hz for the shortest time windows. Pre-event noise windows of the same length as the signal windows are used to compute the SNRs and a threshold equal to 3 is selected to remove noisy spectral ordinates.

3 Method

3.1 Non ergodic ground motion model

The proposed GMM is developed for the geometric mean of horizontal peak ground accelerations (PGA) and 69 FAS ordinates in the frequency range logarithmically equispaced from 0.5 to 25 Hz. The model is calibrated via a mixed-effect regression (Bates, 2015), providing the estimation of the different repeatable effects on the seismic motion (i.e. source, site and path), along with the associated aleatory variability.

We assume the same functional form proposed by Sgobba et al. (2021a) for the response spectrum to describe PGA and spectral ordinates, Y, at each frequency $Y(f)$:

$$log_{10}Y = a + F_M(M) + F_R(M,R) + \delta B_e + \delta S2S_{ref,s} + \delta L2L_{source} + \delta P2P_p + \delta W_0 \qquad [1]$$

where a, $F_M(M)$, $F_R(M,R)$ represent the fixed effects, and δB_e, $\delta S2S_{ref,s}$, $\delta L2L_{source}$, $\delta P2P_p$ stands for zero-mean gaussian-distributed random effects.

Parameter a is the offset and F_M describes the scaling with magnitude:

$$F_M(M) = b_1(M_w - M_h) \text{ for } M \leq M_h,$$

$$F_M(M) = b_2(M_w - M_h) \text{ otherwise.} \qquad [2]$$

Here b_1 and b_2 are calibrated coefficients obtained from nonlinear least-square regression, while M_h is the hinge magnitude fixed at 5.0. The term $F_R(M,R)$ is the other fixed term and represents the scaling with distance:

$$F_R(M,R) = \left[c_1\left(M_w - M_{ref}\right) + c_2\right] log_{10}\frac{\sqrt{R^2+h^2}}{R_{ref}} + c_3(\sqrt{R^2+h^2} - R_{ref}). \qquad [3]$$

$F_R(M,R)$ is divided into a contribution due to the geometrical spreading also computed by nonlinear regression (including magnitude-dependent terms with coefficient c_1, and magnitude-independent with coefficient c_2) and the anelastic attenuation (described by c_3, which is typically regionally dependent). M_{ref} is the reference magnitude obtained from a preliminary nonlinear regression. R_{ref} is the reference distance fixed at 1 km, h is the pseudo depth fixed at 6 km, and R is the Joyner-Boore distance for events larger than 5.5, for which the fault geometry was defined. For lower magnitude events, the Joyner-Boore distance is assumed to be equal to the epicentral distance, since the small area of the rupture surface makes the event equivalent to a point-like source.

The random error terms with respect to the median prediction of the GMM in equation [1] are defined as follows (from Stafford, 2014):

- δB_e is the between-event error, zero mean, normally distributed residuals, which corresponds to the average bias of recordings of one particular earthquake with respect to the prediction of the fixed effects of Eq. 1.

- $\delta S2S_{ref,s}$ is the site-to-site term, defining the systematic bias of ground motions recorded at each station. This term is computed as a reference ground motion level that is observed on a set of reference rock sites, which were previously detected in the study area according to several proxies based on geophysical, seismological and geomorphological features (Lanzano et al., 2020).

- $\delta L2L_{source}$ represents the source term, describing the systematic bias of the source regions (see further).

- $\delta P2P_p$ is the path-term, denoting the systematic deviation along each source-to-site path (from each identified source region to the sites) and being related to anisotropy in the properties of the crustal propagation medium.

Details onboth fixed terms and random terms can be found in Data Availability Statement.

The source regions that are necessary for the computation of systematic terms $\delta L2L_{source}$ and $\delta P2P_p$ were defined by Sgobba et al. (2021a) by performing a spatial-temporal clustering of the events in the dataset using the algorithm proposed by Reasemberg (1985). In particular, these authors identified 6 clusters, 3 of these are located inside our study area (red box in **Fig. 1a**) and are shown in **Fig. 2**. These 3 clusters are (from South to North): cluster #1, including the 6 April 2009 Mw 6.1 L'Aquila, cluster #2, with the 2016 Mw 6.0 Amatrice and Mw 6.5 Norcia sequence, and cluster #3, including 2018 Mw 4.6 Muccia sequence. One of the advantages of the non-ergodic GMM over the ergodic one is the removal of effects due to the different characteristics of the sources, site effects not modelled in the GMM, or isotropic and anisotropic path effects.

As a result, the leftover residuals $\delta \mathrm{W}_0$ reflect the remaining variability unaccounted by Equation [1], which should represent the purely random term unrelated to systematic effects. According to Villani and Abrahamson (2015), the non-systematic effects are connected to the path contributions, while Kotha et al. (2019) associate these remaining record-specific residuals with the four lobes of the S-wave radiation pattern. In our data, the azimuthal pattern of the residuals emerges above the event corner frequency, suggesting its relation to finite source properties (directivity) and not to a point-source feature (radiation pattern).

Therefore, as previously seen in other works (Luzi et al., 2017; Ren et al., 2017; Türker et al., 2022), owing the extensive coverage of the present dataset and taking into account the effects that can be modeled according to the fully non-ergodic functional (Stafford, 2014), we investigate the azimuthal dependence of the $\delta \mathrm{W}_0$ terms to recognize a potential signature of source directivity effects.

3.2 Azimuthal variations of the $\delta W_0(\theta)$ residuals

For each event of the dataset and for each frequency, we analyze the azimuthal variation of the aleatory residuals δW_0. As an example, **Fig. 3** displays the spatial distribution of the PGA aleatory residuals for two M4 events of 30 October 2016 at 11:58:17 (**Fig. 3a**) and 31 October 2016 at 07:05:44 (**Fig. 3b**), both belonging to the 2016-2017 sequence in Central Italy.

Fig. 3a shows a clear spatial pattern with positive values of δW_0 to the South with respect to the epicenter and a well-defined azimuthal distribution (**Fig. 3c**), with peak amplitude of 0.6 at around 180°. Conversely, for the event plotted in **Fig. 3b** the distribution of δW_0 values, ranging between -0.4 and 0.4, are rather random without any predominant direction (**Fig. 3d**). The trend of the aleatory residuals relative to the same events of **Fig. 3** for 4 selected stations, each one located in a different quadrant is plotted in **Fig. 4**.

For the event of 30 October 2016 (**Fig. 4a**), we observe that the station FIAM, located south of the epicenter, is characterized by positive residuals, while MMUR, lying in the northern sector, is affected by negative residuals on the entire frequency range of investigation. The remaining two stations (MCIV and T1241), located in the eastern and western sectors, have similar trends with values spanning around zero. In contrast, for the event of 31 October 2016 (**Fig. 4b**), no significant variations of the δW_0 can be distinguished from the 4 investigated stations. In the whole considered dataset, the cases above are only two illustrative examples, but we have several earthquakes which show different behavior of δW_0 with respect to the frequency: some of these events are shown in **Fig. S1**.

These observations are consistent with directivity effects that can generate spatial patterns, with the largest ground motion amplitude at sites located in the forward-direction with respect to the rupture propagation (Aki and Richards, 1980; Somerville et al., 1997). In light of this, the 30 October 2016 earthquake of **Fig. 3a** and **Fig. 3c** may be classified as a unilateral rupture event, where FIAM station is in the forward-directivity direction, MMUR in the backward-directivity direction, whereas MCIV and T1241 are in neutral positions. Conversely, the event on 31 October 2016 may be classified as a bilateral-rupture event without pronounced source directivity effects.

3.3 Directivity models for $\boldsymbol{\delta W_0(\theta)}$

In order to detect and quantify the directivity effects from the aleatory residuals δW0, we introduce the following model:

$$\delta W_0 = \delta D2D(\theta) + \delta W_{nodir}, \qquad [4]$$

where $\delta D2D(\theta)$ is the function that fits the residuals δW_0 for each event in the dataset as a function of the source-to-site azimuth θ, while δW_{nodir} are the remaining residuals cleared of the directivity effect. Two functional forms are usually adopted to describe the dependence on θ of the $\delta D2D$ term:

i. A cosinusoidal function selected on the basis of the trend of residual distribution with the azimuth θ of the sites (Somerville et al., 1997):

$$\delta D2D(\theta) = Acos(\theta - \theta_0), \qquad [5]$$

where A is the amplitude of the fitting cosine function and θ_0 represents the azimuth at the maximum amplitude.

ii. The directivity coefficient C_d based on a simple theoretical rupture propagation model (Ben-Menahem, 1961; Hirasawa and Stauder, 1965; Ruiz et al., 2011; Pacor et al., 2016a; Gallovič, 2016), which is introduced to account for the rupture propagation on the fault plane. According to Boatwright (2007), the general expression of C_d for a bilateral rupture is the following:

$$C_d = \sqrt{\frac{k^2}{\left[1-\left(\frac{v_r}{c}\right)cos(\theta-\theta_0)\right]^2} + \frac{(1-k)^2}{\left[1+\left(\frac{v_r}{c}\right)cos(\theta-\theta_0)\right]^2}}, \qquad [6]$$

where $\frac{v_r}{c}$ is the Mach number (ratio between rupture and shear-wave velocities, denoted as α in the following), while θ_0 is the azimuth of the rupture direction.
Parameter $k \ \epsilon < 0; 1 >$ represents the relative portion of the rupture length in the direction θ_0. In the case of a unilateral rupture propagating along a narrow fault at a constant velocity v_r, k is equal to 1 and the full expression of C_d reduced to that for the Haskell (1964) model:

$$C_d = \frac{1}{1-(\frac{v_r}{c})cos(\theta-\theta_0)} \qquad [7]$$

Corner frequencies for sites affected by directivity are given by the apparent corner frequency $f_a = f_c C_d(\theta)$, where f_c is proportional to the reciprocal of the rupture duration. Nevertheless, we aim to fit the amplitude of the source spectral ordinates that scale proportionally to C_d^n above frequency f_a, where the exponent n depends on the type of the source model. Omega-squared kinematic rupture models with single corner frequency (e.g., k-squared model by Herrero and Bernard, 1994) suggest $n = 2$, while models with two corner frequencies (e.g., Haskell model, with constant slip and rise time) suggest $n = 1$. In case of purely stochastic models, the directivity disappears and n becomes null (see Gallovič, 2016).

In this second approach, the corrected event-site and path residuals of Eq. 4 are fitted by the following function for each frequency:

$$\delta D2D(\theta) = log_{10}C_d^n(\theta) - < log_{10}C_d^n(\theta) >, \qquad [8]$$

where $< >$ denotes azimuthal averaging. The fitting variables are the angle of the rupture direction θ_0, the ratio k, the Mach number α and the exponent n.

3.4 Tuning of model parameters

In order to determine the fitting parameters, we calibrate the C_d model using the Levenberg-Marquardt optimization algorithm (Marquardt, 1963), which is commonly adopted to solve non-linear least squares problems. In the optimization tests, we assume that the explanatory parameters vary within a fixed range of values: n in the interval between 0 and 2, k between 0.6 and 1, α from 0.5 to 1, and θ_0 in the range 0-360°.

While the fitting of the cosine function is straightforward (Sgobba et al., 2021a), the choice of variables in Eq. 6 should be treated carefully considering a strong trade-off among some of the fitting parameters. In **Fig. 5** and **Tab. 1**, we show an example of the fitting of the residuals for the event of **Fig. 3a**, which is obtained at three different frequencies (results for other sample events are reported in **Fig. S2**).

In fact, although we well resolved the angles related to the direction of propagation θ_0, as shown in Pacor et al. (2016a), similar fitting functions are obtained for different combinations of α and n. Several approaches to deal with this issue have been suggested. Convertito et al. (2017) suggest that the best value is 0.8, after performing a set of inversions for different values ranging between 0.2 and 0.9, selecting as the best model the one resulting in the smallest residual. Ren et al. (2017) suggest that the optimum Mach number α can vary in a range from ~ 0.5 to ~ 1.0, and strongly depends from the value of exponent n considered, as smaller values of n typically result in larger values of the Mach number.

The determination of the optimal values of n still remains ambiguous. In order to automatize the method, the estimation of the values of α, k and n is done by considering the bulk of the events, although the proper option would be to do an event-by-event calibration. Therefore, after the calibration of several tests, we applied a sort of compromise between the resulting values of the inversion algorithm (see **Fig. S3** and **Fig. S4**) and the parameters suggested by literature to have reasonable value even for a physical point of view. The best performance in the majority of the events being able to also capture the trend of the residuals also in the anti-directive azimuths was obtained when fixing k = 0.85 and α = 0.5 (blue curve in **Fig. 5** and case III in **Tab.1**). Since these values are also found to be consistent with common seismological observations (Ren et al., 2017), we decide to adopt this fitting function for the final C_d model.

In **Fig. 6** we inspect the trend of the directivity parameters as a function of frequency for the two events shown in **Fig. 3** (for other examples see **Fig. S5**). As we can observe in **Fig. 6a**, the M4.0 event of 30 October 2016 at 11:58:17 is directive for frequencies greater than 1 Hz as the proxy for the determination coefficient R^2 is consistently greater than 0.5 (third plot at the bottom). For this event, the directivity amplifications is larger than 0.2 and 0.4 if we observe the amplitude A from cosine fitting (black curve) and the value of n (blue curve) from the C_d model, respectively (**Fig. 6a** at the top). In particular, if we look at C_d model (blue curve), we find a maximum value of n around 2.5 corresponding to about 4-5 Hz. The θ_0 angle is very stable and independent of frequency, which is a typical and expected behavior for other directive events.

The direction of the rupture propagation does not change with frequencies (**Fig. 6a** in the middle), while the coefficient of determination R^2 follows the frequency trend of the amplification level and thus can be considered a proxy of the significance of the directivity effects in the ground motions. The M4 event of 31 October 2016 (**Fig. 6b**) shows instead small amplification (< 0.4) at all frequencies both for cosine and C_d models, the θ_0 is unstable and R^2 is consistently below 0.5, indicating that no directivity occurs for this event.

We observed that the C_d function provides slightly better description of the azimuthal variation of the residuals compared to the simpler cosinus-type relationship. The former reproduces better the asymmetry observed in ground motion amplification of directive sites and the de-amplification of non-directive sites. Moreover, it is more related to the physics of the phenomenon, and thus we prefer the C_d model in the subsequent analyses.

4 Results

We apply the above-described method to all the events of the dataset. About 10% of the investigated events (47 out of 456 events) is characterized by median values over frequencies of coefficient of determination $\boldsymbol{R^2}$ and the value of the exponent $\boldsymbol{n}$ for the function $\boldsymbol{C_d}$ are strongly correlated (Pearson coefficient $\boldsymbol{\rho}$ is always greater than 0.7 and, for frequency values greater than 1 Hz, greater than 0.9), as shown by the graph of the correlation coefficient computed for each frequency analyzed in this study (see **Fig. S6**). Since in this research we want to focus on directive events only, we introduce a selection criteria described in the following section.

4.1 Identification of events with significant directivity

Considering that for each event the phenomenon of directivity exhibits variable intensity in different frequency bands of variable length (**Fig. 7**), we introduce some assumptions for identifying a directive event. We designate an event as directive if:

i) The coefficient of determination R^2 is greater than 0.5 for at least 10% of the frequencies investigated (in our case, 7 out of 69 values).

ii) The standard deviation of the angle of the direction of propagation θ_0 is smaller than 20° in the same frequency range.

Fig. 7 shows the values of n as a function of the frequencies analyzed for each event within the magnitude range between 3.7 and 4.0 (for the behavior of n with respect to the other magnitude classes, see **Fig. S7**). Since the frequency ranges analyzed are logarithmically equispaced, the upper part of the graph on x-axis shows the log_2 of the frequency, while the corresponding value of the frequency content is shown at the bottom of the x-axis. After the selection criteria, the directivity frequency-bandwidth can contain gaps, which are in some cases relatively narrow. In order to guarantee the continuity of the frequency-bandwidth with respect the physics of the phenomenon, gaps composed of less than 5 consecutive intervals are filled with the average values in the missing frequency ranges, assuming a tolerance in the R^2 criterion, namely R^2 > 0.45 for closing the gap.

4.2 Directivity event distributions

According to the criteria defined in 4.1, about 36% of the analyzed earthquakes (162 out of 456) can be classified as directive (details about the list of events can be found in Data Availability Statement). The number of the directive events seems independent of magnitude, being distributed as the entire dataset, as illustrated by the histograms reported in **Fig. 8a**. **Fig. 8b** shows the percentage of directive events as a function of frequency for different magnitude ranges (black lines, all events). At low frequencies, this percentage is less than 6% of the total, then increases to about 20% in the range 5-10 Hz, and finally reduces to 10% at higher frequencies. The same trend is visible for events smaller than 4.1 (green and blue lines in **Fig. 8b**), that represent the majority of the catalog. Nevertheless, as the magnitude increases, these effects start to shift to lower frequencies, although the trends are more scattered due to the reduction of the events. Indeed, directivity for moderate events (blue and red curves in **Fig. 8b**) is mainly observed at intermediate frequencies in the band 1.5-10 Hz. For events with magnitude greater than 5 (magenta curve in **Fig. 8b**), more than 30% of the total events exhibit remarkable directivity mainly at lower frequencies ($f \leq 1$ Hz), while this percentage drops starting from 2 Hz.

4.3 Directivity frequency band

As clearly observed in **Fig. 7** and also broadly discussed in other works (Chen et al., 2014; Pacor et al., 2016a; Hirano and Yagi, 2017), the directivity occurs in variable frequency bands that seem to depend on the magnitude of the event. To this purpose, from each directive, we estimate the minimum f_{min} and the maximum frequencies f_{max} corresponding to the values where $R^2 > 0.5$ and plot them as a function of magnitude in **Fig. 9**. There, we also report the corner frequency f_c (blue stars) of the events, estimated by Bindi et al. (2018) who applied a generalized spectral inversion technique (GIT) to a similar dataset in Central Italy.

In order to highlight the dependencies among the various frequencies and magnitude, we plot in **Fig. 9** the median values computed on the half-magnitude bins. While the scatter between f_{min} and f_{max} is relatively large (red and green symbols in **Fig. 9**), binned median values (red and green solid lines in **Fig. 9**) exhibit a decaying trend with increasing magnitude. The decay rate is roughly similar to that of the corner frequency, suggesting a relation of the directivity bandwidth on the source properties (Trugman et al., 2021). Frequencies f_{min} and f_c attain approximately the same values for events with magnitude greater or equal than 4 (although they are only a small proportion of the total events), while for smaller magnitudes the relationship between $log_2 f_{min}$ and $log_2 f_c$

seems constant and equal to about 1.6 log_2 units. We point out that the directivity effect changes the apparent corner frequency as a function of azimuth (Motazedian and Atkinson, 2005; Chen et al., 2014; Pacor et al., 2016a; Bindi et al., 2020). In our analysis this is manifested by increasing directivity amplitude (n) and the coefficient of determination R^2 in the region around the event corner frequency. Nevertheless, in average, f_{min} and f_c are close to each other.

Directivity bandwidth, defined by the ratio between $\frac{f_{max}}{f_{min}}$ in log_2 scale (i.e., number of octaves), is similar for both small and moderate events. This bandwidth is, on average, about 2.3 octaves (i.e. $\frac{f_{max}}{f_{min}} \sim 5$), although this observation may be masked by the limited number of events with M > 4 and the maximum frequency of the dataset at 25 Hz.

This factor is estimated *ad-hoc* for the Central Italy dataset, but there are also theoretical reasons for having the directivity effect scale-dependent. As pointed out in Pacor et al. (2016a), it seems reasonable that at short scales (~5-7 times shorter wavelengths than the rupture size), the rupture propagation is complex, not exhibiting coherent rupture propagation in a single direction and radiating complex wavefield at higher frequencies. Similarly, the wave propagation due to the complexities of the 3-D velocity model may play a significant role in destroying the directivity effect with the seismic waves coming from various parts of the fault becoming less coherent with increasing frequency, although Pacor et al. (2016a) did not observe significant dependence of the residuals on the source distance. We note that the method and the high-quality dataset we use is efficient even at high-frequencies with generally stable at least up to 20 Hz, where the Signal-to-Noise ratio is still high.

In order to validate the directivity detection of each event, we compare our results with those of Wang et al. (2019), who also analyzes the source rupture directivity in the 2016-2017 Central Italy sequence by an independent technique based on a two-step non parametric Generalized Inversion Technique, GIT. **Fig. S8** demonstrates a good agreement of inferred directivity frequency bands.

4.4 Directivity amplitude

As mentioned above, the value of n depends on the type of source model considered, ranging from 0, which represents an incoherent non-directive rupture, to 2, which corresponds to a coherent rupture with the strongest directivity effect. For each event analyzed in this work, we take into account both the peak value n_{max} and the median value n_{med}, computed within the frequency band where $R^2 > 0.5$.

We note that the uncertainty of the n value varies from frequency to frequency, but is relatively small since the ratio between the standard error SE and n is less than 0.5 for 70% of the analyzed directive events for frequency equal to 1 Hz, reaching 97% for frequencies 5 and 10 Hz. A detailed uncertainty analysis is given in **Fig. S9** for several characteristic frequency bands.

As we can observe from the histograms of **Fig. 10**, the median values n_{med} span between 0.26 and 2.1 (median 0.69, mean 0.77), while the maximum values n_{max} vary from 0.8 to 2.8 (median 1.4, mean 1.44). We also note that the largest values of n (above 2) can be alleviated by considering larger rupture velocity (i.e. Mach number) in the fitting procedure. The amplitude of directivity is independent of magnitude, but shows a rather evident linear correlation with the bandwidth of the directivity effects (**Fig. 11**). In particular, the higher is the value of n_{med}, the wider is the frequency band where directivity is observed (see **Fig. S10** for an alternative plot with n_{max}), although the scatter increases.

As shown in **Fig.11**, the linear fit between n_{med} and the ratio $\frac{f_{max}}{f_{min}}$ in logarithmic scale (base 2), is established by the relation:

$$log_2 \frac{f_{max}}{f_{min}} = 2.7427 * n_{med} - 0.1457 \quad [9]$$

The correlation coefficient r, which measures the strength of the linear relationship between n_{med} and bandwidth is 0.7607. In any case, it is important to point out that this relation is valid only for our choice of the fixed parameter values ($k = 0.85$ and $\alpha = 0.5$).

4.5 Direction of rupture propagation

In **Fig. 12,** we show the median value of the direction of rupture propagation, θ_0, over the frequency range where we observe directivity. The distribution is bimodal with two peaks around 150° (SE) and 330° (NW), which are aligned with the fault strikes of the Central Apennines events (D'Amico et al., 2013; Tinti et al., 2016; Improta et al., 2019; Vignaroli et al., 2020).

To support and complement this point, we compare the median of θ_0 with the strike parameters inferred by Herrmann et al. (2011). **Fig. 13a** demonstrates a good match between our rupture and the strikes of the closest plane (fault plane or auxiliary plane): approximately 83% and 45% of the directive analyzed events have a difference less than 45° and 30°, respectively. Nevertheless, some events, mostly with small magnitudes ($M_w < 4.0$), differ significantly from the bisector at 45°, by showing a variation larger than 90°. We point out that the apparent prevalence of rupture directivity in the along-strike direction might be biased due to the ease of detection. Indeed, possible up-dip (or down-dip) rupture propagation along a dipping fault might remain undetected since our analysis is most sensitive to the horizontal rupture propagation.

We also compare our results in terms of direction of rupture propagation with Wang et al. (2019) for 10 most directive events. As shown in **Fig. 13b**, except for 1 event where the values mismatch by approximately 180°, there is a good correspondence between the values of rupture directions obtained by different and independent methods. Similar agreement was found also for the few common events in Pacor et al., 2016a from the L'Aquila sequence.

We try to find a possible relation between the preferential rupture direction (SE or NW) and seismogenic areas or elements connected to the structural geology. We first consider division into source areas following the cluster classification of Sgobba et al., 2021a **(Fig. 2)**, and we do not find any preferred rupture direction. After that, we consider a division based on the recent results from the RETRACE-3D project (Di Bucci et al., 2021, www.retrace3d.it) focused on the revision of all the available geological and geophysical data in the area of the 2016-2018 Central Italy seismic sequence. In particular, we take into consideration one of the major geological structures of the Central Apennines, the Sibillini thrust system **(Fig. 14a)**, which consists of a west-dipping, regional ramp-flat structure over thrusting (Lavecchia, 1985; Pierantoni et al., 2013; Porreca et al., 2018) and divides the investigated zone in the hanging and footwall areas to the north and south, respectively. According to Pizzi et al. (2017), the Mt. Sibillini thrust played a key role as a structural barrier at depth, controlling the rupture of the Mw 6.2 Amatrice event of 24 August 2016 (Chiaraluce et al., 2017) and the initiation of the Mw 6.5 Norcia mainshock of 30 October. In particular, the area struck by the Mw 6.5 seismic sequence has a geo-structural architecture delimited to the East by the deep portion of the Miocene-Pliocene Sibillini thrust system, which according to Buttinelli et al. (2021) is the fault that better matches the hypocentral depth and average rupture dip of the Mw 6.5 mainshock.

In general, according to our results, about 60% of the events lie in the cluster at the North to the Mt. Sibillini, while the remaining ones belong to the hanging wall. Histograms in **Fig. 14b** and relative maps in **Fig. 14c** and **Fig. 14d** suggests that for the hanging wall, the events have a fairly equal distribution of unilateral propagation towards North-West and South-East. Regarding the earthquakes in the footwall, we found a preference of the northward direction of the rupture propagation (44 vs 19 events at the cluster North and South equivalent to about 70% and 30%, respectively). This preferential northward direction of the footwall, that are evident in particular from the aftershocks of the L'Aquila and Amatrice-Visso-Norcia sequences, is in agreement with the findings of Calderoni et al. (2015) and Calderoni et al. (2017), respectively, who investigated the source directivity from azimuthal variation of records using the spectral ratio technique.

5 Discussion

In the following, we introduce a first-order classification of the directive events, based on the relations among the frequency bandwidth $\Delta f = log_2 \frac{f_{max}}{f_{min}}$, the amplitude, proportional to n_{med} and the minimum frequency f_{min} at which the directivity occurs.

To this aim, we plot the distribution of the events on a $f_{min} - \Delta f$ graph (**Fig. 15**), where each data point is colored following of the values of n_{med}. To group the data points in classes representing the "strength" of the directivity, we select three threshold levels following the n_{med} distribution reported in **Fig. 10**. The *weak-directivity* class is relative to $n_{med} < 0.8$ (corresponding to the 65th percentile of the distribution), the *moderate-directivity* class is in the range between 0.8 and 1.3 (around 65th and 95th percentiles) and *high-directivity* class is given by $n_{med} > 1.3$.

One can observe in **Fig. 15** that these three classes are not randomly distributed, but are localized on specific portions of the graph: the weak directivity events are mainly in the bottom part, the moderate ones in the middle, and the high ones lie on the top. This pattern suggests the definition of three domains, delimited by different values of directivity amplitude and frequency bandwidth. The limiting values of Δf are set to the 75th percentile of the corresponding distributions evaluated for each of the three directivity classes, for which we assumed that the median amplitude n_{med} is uniformly distributed over the frequency range.

As we can observe in **Fig. 15**, the first domain is characterized by weak-directivity and small values of Δf, extended up to 1.8 octaves (i.e. *narrow band*), the second one is a "transition" zone, up to 3.4 octaves, formed by the majority of events with moderate directivity and intermediate values of Δf up to 3.4 octaves and a third zone (> 3.4 oct), where we mainly find events characterized by high-directivity and larger Δf (*broadband*).

Such a pattern seems to confirm the existence of a physical correlation between the frequency bandwidth and the strength of directivity so that more directive events tend to show broadband features in contrast to weaker ones that are more bounded in frequency. It is worth to be noted, however, that these findings are strictly related to the statistics of the investigated dataset for Central Italy and that we are also limited in exploring the directivity strength of the smallest events due to the inherent limit of observation, which reaches up to a maximum frequency of 25 Hz (the unexplored domain is displayed with a grey triangle with mesh net in **Fig. 15**).

As an example of application, we consider a scenario earthquake with Mw 4.6 in the study area. Following the seismological relation by Morasca et al. (2019) calibrated for Central Italy, this magnitude corresponds to a corner frequency f_c approximately equal to 1 Hz, that can be assumed equal to f_{min} according to the trend illustrated in **Fig. 9**. Based on the above findings, this f_{min} may correspond to different frequency bandwidths according to the level of n_{med} (black dashed lines in **Fig. 15**). For instance, an event with weak-directivity (n_{med} = 0.55) is characterized by a directivity bandwidth ranging from f_{min} equal to 1 Hz up to 3 Hz (Δf = 1.55 octaves according to **Eq. 9**). On the other hand, for an high-directivity event with n_{med} = 1.55, we get a value of bandwidth Δf = 4.1 octaves (red cross in **Fig. 15**), which means that in this case directivity appears from 1 to about 18 Hz.

6 Conclusions

In this work we have shown a statistical overview aiming to provide a better understanding of the main features of the rupture directivity based on empirical evidence of seismological observations. The study exploits the exceptionally dense dataset of Central Italy compiled after the main sequences of L'Aquila in 2009 and Amatrice-Visso-Norcia from 2016 to 2018 with a large number of recordings and broad azimuthal coverage.

We take advantage of this dataset to calibrate an *ad-hoc* fully non-ergodic FAS-GMM adopted as a reference model for the target area. The non-ergodicity enables removal of event-, site- and path-related components of variability in the ground motion model to isolate the aleatory effects related to source directivity. The aleatory residuals exhibit a clear azimuthal pattern and frequency dependence, representing the signature of source directivity, in agreement with previous studies (Pacor et al., 2016a; Luzi et al., 2017; Sgobba et al., 2021a). The residuals are well fitted by the physics-based directivity function $\boldsymbol{C_d^n(\theta)}$, including their asymmetry in amplification of directive and anti-directive sites.

Parameters of the $\boldsymbol{C_d^n(\theta)}$ fitting function are the Mach number $\boldsymbol{\alpha}$ (ratio between the rupture velocity and the shear-wave velocity), the $\boldsymbol{k}$ parameter (the portion of the rupture length in the propagation direction), and the angle $\boldsymbol{\theta_0}$ representing the direction of the rupture propagation. The strength of the azimuthal variability of ground motions is proportional to exponent $\boldsymbol{n}$, i.e. parameter describing the "strength" of the directivity. Optimization tests confirmed the existence of a strong trade-off among the directivity parameters. We thus fixed some of them at typically accepted values in seismological applications: $\boldsymbol{k} = 0.85$, $\boldsymbol{\alpha} = 0.5$. We prefer to allow $\boldsymbol{n}$ to possibly depend on frequency, as it is theoretically more acceptable than frequency dependence of the rupture velocity.

Statistical investigation of directivity parameters for the whole dataset demonstrated strong dependence of the exponent $\boldsymbol{n}$ and the coefficient of determination $\boldsymbol{R^2}$. On this basis, we classify the events in the dataset as "directive" and "non-directive" according to $\boldsymbol{R^2}$ as a statistical *proxy*, assuming that the directivity effect is significant when $\boldsymbol{R^2}$ is greater than 50%. The directive events represent 36% of the whole dataset. The main results are:

- The azimuthal distribution of the directive events is bimodal with two peaks at 150° and 330°, corresponding to the NW-SE structural orientation of the Central Apennines fault systems. Although the prevailing directivity directions are aligned with the strikes of the earthquakes only, events with possibly up-dip or down-dip rupture propagation would remain rather undetected by our method.
- No preferential direction of directivity is present in the whole dataset. Nevertheless, the Amatrice sector is dominated by events with N-NW rupture propagation (70%). We speculate that the main structural discontinuity of the region (i.e. the Mt. Sibillini thrust) may place constraints on the location of the nucleation point, as shown also by Calderoni

et al. (2017) for the 2016-2017 seismic sequence of Central Italy. However, the present results need more extensive correlations with rheological parameters to be confirmed.

- The observed directivity is a band-limited phenomenon. It occurs always above the corner frequency up to a maximum value f_{max}. We propose a relation between the directivity amplitude n and the directivity bandwidth (Eq. 9). For example, for a moderate directivity (n=0.9), the bandwidth spans up to 5 times the minimum frequency f_{min}. We note that the result is partially only an extrapolation for smaller events, because we are limited by the maximum investigated frequency of 25 Hz.

We point out that our observed band-limited directivity effect cannot be easily explained by a simple azimuthally-dependent stretching of the apparent source times functions identified by time-domain methods (e.g., Warren and Silver, 2006; Abercrombie et al., 2017; Yin et al., 2021). Indeed, when we move from the time to the frequency domain, the apparent duration stretching causes contraction of the spectrum, including a shift of the corner frequency f_c. The directivity would thus affect the spectral amplitudes at all frequencies beyond the minimum apparent f_c. It means that the observed limited directivity bandwidth should be due to other phenomenon, possibly related to small-scale complexity of the rupture evolution.

Our quantification of the frequency-dependent directivity effect on the ground motions represents a first step towards its empirical parameterization, since it connects the bandwidth of significant directivity with the fundamental scenario parameters. In particular, we can use the directivity function $C_d^n(\theta)$ for predictive purposes, by setting θ_0 and n and calculating the directivity bandwidth from Eq. 9. The minimum directivity frequency can be approximated by the corner frequency calculated from the stress drop and magnitude using seismological scaling laws.

This effort to incorporate the directivity contributions into empirical GMMs was carried out because past investigations performed in the NGA-West2 project (Spudich and Chiou, 2008; Spudich, 2014) led to the conclusion that ‘none of these models has a functional form that transitions smoothly from large to small magnitude and that describes the small-magnitude or short-period directivity’. Our results may provide useful insights to move towards parametrization of directivity within the empirical simulation of shaking scenarios in Central Italy, as the ones proposed by Sgobba et al. (2021a) in the non-ergodic framework. Nevertheless, we clarify that the proposed approach reproduces well the characteristics of the data in the target region while more extensive research is needed to generalize these findings.

Data Availability Statement

All the data used for Central Italy (*CI_dataset*) can be found at the page: https://shake.mi.ingv.it/central-italy/. In particular, for this analysis, coefficients and uncertainty terms of the non-ergodic FAS ground motion model *CI-FAS_GMM6* (Lanzano et al., 2022, https://doi.org/10.13127/ci_dataset/CI-FAS_GMM) and the directivity characteristics of the 162 events *CI-FAS_directivity* (Colavitti et al., 2022; https://doi.org/10.13127/ci_dataset/CI-FAS_directivity) are publicly available. The data on the strikes of fault and auxiliary plane, with which we compared the median values obtained in this research are available at https://www.eas.slu.edu/eqc/eqc_mt/MECH.IT.

Acknowledgements

We are very grateful to Prof. Daniele Spallarossa (University of Genova, Italy) for making the dataset used in this work available. This research is supported by *Istituto Nazionale di Geofisica e Vulcanologia* (INGV) in the frame of the project *Pianeta Dinamico* (Working Earth) - Geosciences for the Understanding of the Dynamics of the Earth and the Consequent Natural Risks (CUP code D53J19000170001), founded by the Italian Ministry of University and Research (MIUR) in the Task S3 - 2021 - Seismic attenuation and variability of seismic motion. Moreover, this study has been partially funded by INGV-DPC Agreement B1 2019-2021, with the goal of promoting research activities in the field of seismic hazard in Italy. We are very grateful to the Editor Prof. Rachel E. Abercrombie, an anonymous reviewer and Prof. Yefei Ren for their valuable comments that improved this manuscript. All the authors declare that the research was conducted in the absence of any commercial or financial relationships that could be construed as a potential conflict of interest.

References

Abercrombie, R. E., Poli, P., and Bannister, S. (2017). Earthquake directivity orientation, and stress drop within the subducting plate at the Hikurangi margin, New Zeland. *J. Geophys. Res. Solid Earth, 122,10, 176-10, 188*. 4. https://doi.org/10.1002/2017JB014935.

Abrahamson, N. A., Somerville, P. G. (1996). Effects of the hanging wall and footwall on ground motions recorded during the Northridge earthquake. *Bull. Seismol. Soc. Am*., 86(1B), S93-S99. https://doi.org/10.1785/BSSA08601B0S93.

Abrahamson, N. A., Kuehn, N., Walling, M., and Landwehr, N. (2019). Probabilistic Seismic Hazard Analysis in California Using Nonergodic Ground-Motion Models. *Bull. Seism. Soc. Am*., 109(4), 1235-1249. https://doi.org/10.1785/0120190030.

Aki, K., and Richards, P., 1980. Quantitative Seismology: Theory and Methods. W. H. Freeman.

Ameri, G., Massa, M., Bindi, D., D'Alema, E., Gorini, A., Luzi, L., Marzorati, S., Pacor, F., Paolucci, R., Puglia, R., and Smerzini, C. (2009). The 6 April 2009 Mw 6.3 L'Aquila (Central Italy) Earthquake: strong-motion observations. *Seismol. Res. Lett*., 80 (6), 951-966. https://doi.org/10.1785/gssrl.80.6.951.

Anderson, J. G. (2007). Earthquake Seismology - Physical processes that control strong ground motion. In *Treatise on Geophysics, 2nd Edition.* Elsevier.

Baltay, A. S., Hanks, T. C., and Abrahamson, N. A. (2017). Uncertainty, variability, and earthquake physics in ground-motion prediction equations. *Bull. Seismol. Soc. Am*., 107(4), 1754-1772. https://doi.org/10.1785/0120160164.

Bates, D., Mächler, B., Bolker, B., and Walker, S. (2015). Fitting linear mixed-effects models using lme4, 2015. *J. Stat. Software*, 67(1), 1-48. https://doi.org/10.18637/jss.v067.i01.

Ben-Menahem, A. (1961). Radiation of seismic surface waves from finite moving sources. *Bull. Seismol. Soc. Am., 51*, 401- 435.

Bernard, P., and A. Herrero (1994). Slip heterogeneity, body-wave spectra, and directivity of earthquake ruptures. *Ann. Geofis., 37*, 1679-1690. https://doi.org/10.4401/ag-4159.

Bernard, P., Herrero, A., and Berge, C. (1996). Modelling directivity of heterogeneous earthquake ruptures. *Bull. Seism. Soc. Am., 86*, 1149-1160. https://doi.org/10.1785/BSSA0860041149.

Bindi, D., Spallarossa, D., Picozzi, M., Scafidi, D., and Cotton, F. (2018). Impact of Magnitude Selection on Aleatory Variability Associated with Ground-Motion Predictions Equations: Part I - Local, Energy, and Moment Magnitude Calibration and Stress-Drop Variability in Central Italy. *Bull. Seismol. Soc. Am., 108(3A)*, 1427-1442.https://doi.org/10.1785/0120170356.

Bindi, D., Spallarossa, D., Picozzi, M., and Morasca, P. (2020). Reliability of Source Parameters for Small Events in Central Italy: Insights from Spectral Decomposition Analysis Applied to Both Synthetic and Real Data. *Bull. Seism. Soc. Am., 110 (6)*, 3139-3157. https://doi.org/10.1785/0120200126.

Boatwright, J., (2007). The persistence of directivity in small earthquakes. *Bull. Seismol. Soc. Am.*, *97*, 1850-1861. https://doi.org/10.1785/0120050228.

Boncio, P., Brozzetti, F., and Lavecchia, G. (2000). Architecture and seismotectonics of a regional low-angle normal fault zone in central Italy. *Tectonics, 19(6)*, 1038-1055. https://doi.org/10.1029/2000TC900023.

Bonini, L., Maesano, F. E., Basili, R., Burrato, P., Carafa, M. M. C., Fracassi, U., Kastelic, V., Tarabusi, G., Tiberti, M. M., Vannoli, P.., and Valensise, G. (2016). Imaging the tectonic framework of the 24 August 2016, Amatrice (central Italy) earthquake sequence: new roles for old players? *Ann. Geophys. 59*. https://doi.org/10.4401/AG-7229.

Buttinelli, M., Petracchini, L., Maesano, F. E., D'Ambrogi, C., Scrocca, D., Marino, M., Capotorti, F., Bigi, S., Cavinato, G. P., Mariucci, M. T., Montone, P., and Di Bucci, D. (2021). The impact of structural complexity, fault segmentation, and reactivation on seismotectonics: Constraints from the upper crust of the 2016-2017 Central Italy seismic sequence area. *Tectonophysics*, 810, 228861. https://doi.org/10.1016/j.tecto.2021.228861.

Calderoni, G., Rovelli, A., Ben-Zion, Y., and Di Giovambattista, R. (2015). Along-strike rupture directivity of earthquakes of the 2009 L'Aquila, Central Italy, seismic sequence. *Geophys. J. Int.*, *205*, 399-415. https://doi.org/10.1093/gji/ggv275.

Calderoni, G., Rovelli, A., and Di Giovambattista, R. (2017). Rupture directivity of the strongest 2016-2017 Central Italy earthquakes. *J. Geophys. Res. Solid Earth*, *122(11)*, 9118-9131. https://doi.org/10.1002/2017JB014118.

Carafa, M. C., and Barba, S. (2011). Determining rheology from deformation data: The case of central Italy. *Tectonics*, *30 (2)*. https://doi.org/10.1029/2010TC002680.

Chen, P., Jordan, T. H., and Zhao, L. (2010). Resolving fault plane ambiguity for small earthquakes. *Geophys. J. Int.*, *181*, 493-501. https://doi.org/10.1111/j.1365-246X.2010.04515.x.

Chen, Y., Letort, J., Cotton, F., and Drouet, S. (2014). High-frequency directivity effects: evidence from analysis of the Les Saintes records. *J. Seismol*., 18, 457-466. https://doi.org/10.1007/s10950-014-9419-2.

Chiarabba, C., Amato, A., Anselmi, M., Baccheschi, P., Bianchi, I., Cattaneo, M., Cecere, G., Chiaraluce, L., Ciaccio, M. G., De Gori, P., De Luca, G., Di Bona, M., Di Stefano, R., Faenza, L., Govoni, A., Improta, L., Lucente, F. P., Marchetti, A., Margheriti, L., Mele, F., Michelini, A., Monachesi, G., Moretti, M., Pastori, M., Piana Agostinetti, N., Piccinini, D., Roselli, P., Seccia, D., and Valoroso, L. (2009). The 2009 L'Aquila (Central Italy) Mw6.3 earthquake: Main shock and aftershocks. *Geophys. Res. Lett.*, *36*, L18308. https://doi.org/10.1029/2009GL039627.

Chiarabba, C., De Gori, P., Cattaneo, M., Spallarossa, D. and Segou, M. (2018). Faults Geometry and the Role of Fluids in the 2016-2017 Central Italy Seismic Sequence. *Geophys. Res. Lett. 45 (14)*, 6963-6971. https://doi.org/10.1029/2018GL077485.

Chiaraluce, L., Di Stefano, R., Tinti, E., Scognamiglio, L., Michele, M., Casarotti, E.. Cattaneo, M., De Gori, P., Chiarabba, C., Monachesi, G., Lombardi, A., Valoroso, L., Latorre, D., and Marzorati, S. (2017). The 2016 Central Italy Seismic Sequence: A First Look at the Mainshocks, Aftershocks, and Source Models. *Seismol. Res. Lett. 88 (3)*, 757-771. https://doi.org/10.1785/0220160221.

Chioccarelli, E. and Iervolino, I. (2014). Sensitivity analysis of directivity effects on PSHA. *Boll. Geof. Teor. Appl.*, *55(1)*, 41-53. https://doi.org/0.4430/bgta0099.

Colavitti, L., Lanzano, G., Sgobba, S., and Pacor, F. (2022). CI-FAS_Directivity: List of earthquakes with evidence of directivity in Central Italy [Data set]. Istituto Nazionale di Geofisica e Vulcanologia (INGV). https://doi.org/10.13127/ci_dataset/CI-FAS_directivity *(in validation phase).*

Convertito, V., Catalli, F., and Emolo, A. (2013). Combining stress transfer and source directivity: the case of the 2012 Emilia seismic sequence. *Sci. Rep*. 3, 3114. https://doi.org/10.1038/srep03114.

Convertito, V., Pino, N. A., and Di Luccio, F. (2016). Investigating source directivity of moderate earthquakes by multiple approach: the 2013 Matese (southern Italy) Mw=5 event. *Geophys. J. Int.*, *207*, 1513-1528. https://doi.org/10.1093/gji/ggw360.

Convertito, V., De Matteis, R., and Pino, A. (2017). Evidence for Static and Dynamic Triggering of Seismicity Following the 24 August 2016, Mw = 6.0, Amatrice (Central Italy) Earthquake. *Pure Appl. Geophys., 174,* 3663-3672. https://doi.org/10.1007/s00024-017-1559-1.

Courboulex, F., Dujardin, A., Vallee, M., Delouis, B., Sira, C., Deschamps, A. Honore, L. and Thouvenot, F. (2013). High-frequency directivity effect for an Mw 4.1 earthquake, widely felt by the population in southeastern France. *Bull. Seismol. Soc. Am., 103,* 3347-3353. https://doi.org/10.1785/0120130073.

D'Amico, S., Orecchio, B., Presti, D., Neri, G., Wu, W.-N., Sandu, I., Zhu, L. and Hermann, R. B. (2013). Source parameters of small and moderate earthquakes in the area of the 2009 L'Aquila earthquake sequence (Central Italy). *Phys. Chem. Earth*, 63, 77-91. https://doi.org/10.1016/j.pce.2013.02.005.

Di Bucci, D., Buttinelli, M., D'Ambrogi, C., Scrocca, D., and the RETRACE-3D Working Group, (2021). RETRACE-3D project: a multidisciplinary collaboration to build a crustal model for the 2016-2018 Central Italy seismic sequence. *Boll. di Geofis. Teor. ed Appl., 62(1),* 1-18. https://doi.org/10.4430/bgta0343.

Di Luccio, F., Ventura, G., Di Giovambattista, R., Piscini, A., Cinti, F. R. (2010). Normal faults and thrusts reactivated by deep fluids: The 6 April 2009 Mw 6.3 L'Aquila earthquake, central Italy. *J. Geophys. Res. Solid Earth, 115,* B06315. https://doi.org/10.1029/2009JB007190.

Dreger, D. (1994). Empirical Green's function study of the January 17, 1994 Northridge, California earthquake. *Geophys. Res. Lett*., 21(24), 2633-2636. https://doi.org/10.1029/94GL02661.

Douglas, A., Hudson, J. A., and Pearce, R. G. (1988). Directivity and the Doppler effect. *Bull. Seismol. Soc. Am., 78 (3),* 1367-1372.

Folesky, J., Kummerow, J., Shapiro, S. A., Häring, M., and Asanuma, H. (2016). Rupture directivity of fluid-induced microseismic events: Observations from an enhanced geothermal system. *J. Geophys. Res. Solid Earth, 121*, 8034-8047. https://doi.org/10.1002/2016JB013078.

Gallovič, F. (2016). Modeling Velocity Recordings of the Mw 6.0 South Napa, California, Earthquake: Unilatel Event with Weak High-Frequency Directivity. *Seismol. Res. Lett., 87(1),* 2-14. https://doi.org/10.1785/0220150042.

Haskell, N. (1964). Total energy and energy spectral density of elastic wave radiation from propagating faults. *Bull. Seism. Soc. Am., 54 (6A)*, 1811-1841.

Herrero, A., and Bernard, P. (1994). A kinematic self-similar rupture process for earthquakes. *Bull. Seism. Soc. Am., 84(4)*, 1216-1228. https://doi.org/10.1785/BSSA0840041216.

Herrmann, R. B., Malagnini, L., and Munafò, I. (2011). Regional Moment Tensors of the 2009 L'Aquila Earthquake Sequence. *Bull. Seism. Soc. Am., 101 (3)*, 975-993. https://doi.org/10.1785/0120100184.

Hirano, S., and Yagi, Y. (2017). Dependence of seismic and radiated energy on shorter wavelength components. *Geophys. J. Int., 209*, 1585-1592. https://doi.org/10.1093/gji/ggx108.

Hirasawa, T., and Stauder, W. (1965). On the seismic body waves from a finite moving source. *Bull. Seism. Soc. Am., 55(2)*, 237-262.

Improta, L., Latorre, D., Margheriti, L., Nardi, A., Marchetti, A., Lombardi, A. M., Castello, B., Villani, F., Ciaccio, M. G., Mele, F. M., Moretti, M., and The Bollettino Sismico Italiano WG (2019). *Sci. Rep., 9*, 6921. https://doi.org/10.1038/s41598-019-43393-2.

Joyner, W. (1991). Directivity for non-uniform ruptures. *Bull. Seismol. Soc. Am., 81*, 1391-1395. https://doi.org/10.1785/BSSA0810041391.

Konno, K., and Ohmachi, T. (1998). Ground-motion characteristics estimated from spectral ratio between horizontal and vertical components of microtremor. *Bull. Seism. Soc. Am., 88(1)*, 228-241. https://doi.org/10.1785/BSSA0880010228.

Kotha, S. R., Cotton, F., and Bindi, D. (2019). Empirical Models of Shear-Wave Radiation Pattern Derived from Large Datasets of Ground-Shaking Observations. *Sci. Rep., 9*, 981. https://doi.org/10.1038/s41598-018-37524-4.

Kuehn, N. M., Abrahamson, N. A., and Walling, M. A. (2019). Incorporating Nonergodic Path Effects into the NGA-West2 Ground-Motion Prediction Equations. *Bull. Seism. Soc. Am. 109(2)*, 575-585. https://doi.org/10.1785/0120180260.

Lavecchia, G. (1985). Il sovrascorrimento dei Monti Sibillini: analisi cinematica e strutturale. *Boll. Soc. Geol. Ital., 104*, 161-194.

Lanzano, G., Pacor, F., Luzi, L., D'Amico, M., Puglia, R., and Felicetta, C. (2017). Systematic source, path and site effects on ground motion variability: the case study of Northern Italy. *Bull. Earthq. Eng. 15(11)*, 4563-4583. https://doi.org/10.1007/s10518-017-0170-2.

Lanzano, G., Felicetta, C., Pacor, F., Spallarossa, D., and Traversa, P. (2020). Methodology to identify the reference rock sites in regions of medium-to-high seismicity: an application in Central Italy. *Geophys. J. Int. 222(3)*, 2053-2067. https://doi.org/10.1093/gji/ggaa261.

Lanzano, G., Colavitti, L., Sgobba, S., Spallarossa, D., and Pacor, F. (2022). CI-FAS_GMM: Ground Motion Model of the Fourier Amplitude Spectrum ordinates for the shallow active crustal events in Central Italy [Data set]. Istituto Nazionale di Geofisica e Vulcanologia (INGV). https://doi.org/10.13127/CI_dataset/CI-FAS_GMM (*in validation phase*).

Lavrentiadis, G., Abrahamson, N. A., and Kuehn, N. M. (2021). A non-ergodic effective amplitude ground-motion model for California. *Bull. Earthq. Eng*., 1573-1456. https://doi.org/10.1007/s10518-021-01206-w.

López-Comino, J. A., de Lis Mancilla, F., Morales, J., and Stich, D. (2012). Rupture directivity of the 2011, Mw 5.2 Lorca earthquake (Spain). *Geophys. Res. Lett. 39*: L03301. https://doi.org/10.1029/2011GL050498.

López-Comino, J. A., Cesca, S., Niemz, P., Dahm, T. and Zang, A. (2021). Rupture Directivity in 3D Inferred From Acoustic Emissions Events in a Mine-Scale Hydraulic Fracturing Experiment. *Front. Earth. Sci. 9*: 670757. https://doi.org/10.3389/feart.2021.670757.

Luzi, L., Pacor, F., Puglia, R., Lanzano, G., Felicetta, C., D'Amico, M., Michelini, A., Faenza, L., Lauciani, V., Iervolino, I., Baltzopoulos, G., and Chioccarelli, E. (2017). The Central Italy seismic sequence between August and December 2016: analysis of strong-motion observations. *Seismol Res Lett., 88(5)*: 1219-1231. https://doi.org/10.1785/0220170037.

Marquardt, D. (1963). An Algorithm for Least-Squares Estimation of Nonlinear Parameters. In *SIAM Journal on Applied Mathematics. 11 (2)*, 431-441.

McGuire, J. J. (2004). Estimating finite source properties of small earthquake ruptures. *Bull Seismol Soc Am., 94(2)*, 377-393. https://doi.org/10.1785/0120030091.

Morasca, P., Walter, W. R., Mayeda, K., and Massa, M. (2019). Evaluation of earthquake stress parameters and its scaling during the 2016-2017 Amatrice-Norcia-Visso sequence - Part I. *Geophys J. Int.*, 218 (1), 446-455. https://doi.org/10.1093/gji/ggz165.

Motazedian, D., and Atkinson, G. M. (2005). Stochastic finite-fault modeling based on a dynamic corner frequency. *Bull. Seism. Soc. Am.*, *95*(3), 995-1010. https://doi.org/ 10.1785/0120030207.

Pacor, F., Cultrera, G., Mendez, A., and Cocco, M. (2005). Finite fault modeling of strong ground motions using a hybrid deterministic-stochastic approach. *Bull. Seism. Soc. Am.*, *95*, 225-240. https://doi.org/10.1785/0120030163.

Pacor, F., Gallovič, F., Puglia, R., Luzi, L., and D'Amico, M. (2016a). Diminishing high-frequency directivity due to a source effects: empirical evidence from small earthquakes in the Abruzzo region, Italy. *Geophys Res Lett.: Solid Earth, 43,* 5000-5008. https://doi.org/10.1002/2016GL068546.

Pacor, F., Spallarossa, D., Oth, A, Luzi, L., Puglia, R., Cantore, L., Mercuri, A., D'Amico, M., and Bindi, D. (2016b). Spectral models for ground motion prediction in the L'Aquila region (Central Italy): evidence for stress-drop dependence on magnitude and depth. *Geophys. J. Int*., 204, 697-718. https://doi.org/10.1093/gji/ggv448.

Pacor, F., Felicetta, C., Lanzano, G., Sgobba, S., Puglia, R., D'Amico, M., Russo, E., Baltzopoulos, G., Iervolino, I. (2018). NESS1: A WorldWide Collection of Strong-Motion Data to Investigate Near-Source Effects. *Seismol. Res. Lett. 89(6),* 2299-2313. https://doi.org/10.1785/0220180149.

Pierantoni, P., Deiana, G., Galdenzi, S. (2013). Stratigraphic and structural features of the Sibillini mountains, Umbria-Marche Apennines (Italy). *Ital. J. Geosci*., 132 (3), 497-520. https://doi.org/10.3301/IJG.2013.08.

Pizzi, A., Di Domenica, A., Gallovič, F., Luzi, L., and Puglia, R. (2017). Fault segmentation as constraint to the occurrence of the main shocks of the 2016 Central Italy seismic sequence. *Tectonics*, *36*, 2370–2387. https://doi.org/10.1002/2017TC004652.

Porreca, M., Fabbrizzi, A., Azzaro, S., Pucci, S., Del Rio, L., Pierantoni, P. P., Giorgetti, C., Roberts, G., and Barch, M. R. (2020). 3D geological reconstruction of the M. Vettore seismogenic fault system (Central Apennines, Italy): Cross-cutting relationship with the M. Sibillini thrust. *J. Struct. Geol*., 131, 103938. https://doi.org/10.1016/j.jsg.2019.103938.

Reasenberg, P. (1985) Second-order moment of Central California seismicity, 1969-1982. *J. Geophys. Res. Solid Earth*, 90 (B7), 5479-5495. https://doi.org/10.1029/JB090iB07p05479.

Ren, Y., Wang, H., and Wen, R. (2017). Imprint of rupture directivity from ground motions of the 24 August 2016 Mw6.2 Central Italy earthquake. *Tectonics, 36*, 3178-3191. https://doi.org/10.1002/2017TC004673.

Ross, Z. E., Trugman, D. T., Azizzadenesheli, K. and Anandkumar, A. (2020). Directivity modes of earthquake populations with unsupervised learning. *J. Geophys. Res. Solid Earth,* 125, e2019JB018299. https://doi.org/10.102972019JB018299.

Rowshandel, B. (2010). Directivity correction for the Next Generation Attenuation (NGA) relations. *Earthq. Spectra, 26(2)*, 525-559. https://doi.org/10.1193/1.3381043.

Ruiz, J. A., Baumont, D., Bernard, P., and Berge-Thierry, C. (2011). Modelling directivity of strong ground motion with a fractal, k^{-2}, kinematic source model. *Geophys. J. Int., 186(1)*, 226-244. https://doi.org/10.1111/j.1365-246X.2011.05000.x.

Sahakian, V. J., Baltay, A., Hanks, T. C., Buehler, J., Vernon, F. L., Kilb, D., and Abrahamson, N. A. (2019). Ground motion residuals, path effects, and crustal properties: A pilot study in Southern California. *J. Geophys. Res. Solid Earth, 124*. https://doi.org/10.1029/2018JB016796.

Seekins, L. C., and Boatwright, J. (2010). Rupture directivity of moderate earthquakes in northern California. *Bull. Seism. Soc. Am, 100*, 1107-1119. https://doi:10.1785/0120090161.

Sgobba, S., Lanzano, G., and Pacor, F. (2021). Empirical nonergodic shaking scenarios based on spatial correlation models: An application to central Italy. *Earthq. Eng. Struct. D., 50(1)*, 60-80. https://doi.org/10.1002/eqe.3362.

Sgobba, S., Felicetta, C., Lanzano, G., Ramadan, F., D'Amico, M., and Pacor, F. (2021b). NESS2.0: An Updated Version of the Worldwide Dataset for Calibrating and Adjusting Ground-Motion Models in Near Source. *Bull. Seism. Soc. Am., 111(5)*, 2358-2378. https://doi.org/10.1785/0120210080.

Sgobba, S., Lanzano, G., Pacor, F., and Felicetta, C. (2021c). An empirical model to account for spectral amplification of pulse-like ground motion records. *Geosciences, 11(1)*, 15. https://doi.org/10.3390/geosciences11010015.

Shahi, S. K., and Baker, J. W. (2011). An Empirically Calibrated Framework for Including the Effects of Near-Fault Directivity in Probabilistic Seismic Hazard Analysis. *Bull. Seism. Soc. Am. 101(2)*, 742-755. https://doi.org/10.1785/0120100090.

Somerville, P. G., Graves, R. W., and Smith, N. F. (1996). Forward rupture directivity in the Kobe and Northridge earthquakes, and implications for structural engineering. *Seismol. Res. Lett., 67*, 55.

Somerville, P., Smith, N. F., Graves, W., and Abrahamson, N. (1997). Modification of empirical strong ground motion attenuation relations to include the amplitude and duration effects of rupture directivity. *Seismol. Res. Lett., 68*, 199-222. https://doi.org/10.1785/gssrls.68.1.199.

Spagnuolo, E., Herrero, A., and Cultrera, G. (2012). The effect of directivity in a PSHA framework. *Geophys. J. Int.*, *191*, 616-626. https://doi.org/10.1111/j.1365-246X.2012.05630.x.

Spudich, P., and Chiou, B. (2008). Directivity in NGA earthquake ground motions; analysis using isochrone theory. *Earthquake Spectra*, 24, 279-298. https://doi.org/10.1193/1.2928225.

Spudich, P., Rowshandel, B., Shahi, S., Baker, J. W., M. EERI. and Chiou, B., S.-J. (2014). Comparison of NGA-West2 Directivity Models, *Earthquake Spectra 30*, 1199-1221. https://doi.org/10.1193/080313EQS222M.

Stafford, P. J. (2014). Crossed and nested mixed-effects approaches for enhanced model development and removal of the ergodic assumption in empirical ground-motion models. *Bull. Seismol. Soc. Am. 104(2)*, 702-719. https://doi.org/10.1785/0120130145.

Tan, Y., and Helmberger, D. (2010). Rupture directivity characteristics of the 2003 Big Bear sequence. *Bull. Seismol. Soc. Am.*, *100(3)*, 1089-1106. https://doi.org/10.1785/0120090074.

Tinti, E., Scognamiglio, L., Michelini, A., and Cocco, M. (2016). Slip heterogeneity and directivity of the ML 6.0. Amatrice earthquake estimated with rapid finite-fault inversion. *Geophys. Res. Lett.*, *43*, 10745-10752. https://doi.org/10.1002/2016GL071263.

Tomic, J., Abercrombie, R. E., and Do Nascimento, A. (2009). Source parameters and rupture velocity of small $M \leq 2.2$ reservoir induced earthquakes. *Geophys. J. Int.*, *179*, 1013-1023. https://doi.org/10.1111/j.1365-246X.2009.04233.x.

Trugman, D. T., S. X. Chu, and V. C. Tsai (2021). Earthquake Source Complexity Controls the Frequency Dependence of Near-Source Radiation Patterns. *Geophys. Res. Lett. 48*, e2021GL095022. https://doi.org/10.1002/essoar.10507460.1.

Trugman, D. T. (2022). Resolving differences in the rupture properties of M5 earthquakes in California using Bayesian source spectral analysis. *J. Geophys. Res. Solid Earth*, 127, e2021JB023526. https://doi.org/10.1029/2021JB023526.

Türker, E., Cotton, F., Pilz, M., Weatherill, G. (2022). Analysis of the 2019 Mw 5.8 Silivri Earthquake Ground Motions: Evidence of Systematic Azimuthal Variations Associated with Directivity Effects. *Seismol. Res. Lett.*, *XX*, 1-13. https://doi.org/10.1785/0220210168.

Velasco, A. A., Ammon, C. J., and Lay, T. (1994). Empirical Green function deconvolution of broadband surface waves: Rupture directivity of the 1992 Landers, California (Mw = 7.3) earthquake. *Bull. Seism. Soc. Am, 84(3),* 735-750. https://doi.org/10.1785/BSSA0840030735.

Vignaroli, G., Mancini, M., Brilli, M., Bucci, F., Cardinali, M., Giustini, F., Voltaggio, M., Yu, T. L., and Shen, C. C. (2020). Spatial-temporal evolution of extensional faulting and fluid circulation in the Amatrice Basin (Central Apennines, Italy) during the Pleistocene. *Front. Earth. Sci.*, *8*, 130. https://doi.org/10.3389/feart.2020.00130.

Villani, M., and Abrahamson, N. A. (2015). Repeatable Site and Path Effects on the Ground-Motion Sigma Based on Empirical Data from Southern California and Simulated Waveforms from the CyberShake Platform. *Bull. Seismol. Soc. Am. 105 (5)*, 2681-2695. https://doi.org/10.1785/0120140359.

Walters, R. J., Elliott, J. R., D'Agostino, N., England, P. C., Hunstad, I., Jackson, J. A., Parsons, B., Phillips, R. J. and Roberts, G. (2009). The 2009 L'Aquila earthquake (Central Italy): A source mechanism and implications for seismic hazard. *Geophys. Res. Lett.*, *36*, L17312. https://doi.org/10.1029/2009GL039337.

Warren, L. M., and Silver, P. G. (2006). Measurement of differential rupture durations as constraints on the source finiteness of deep-focus earthquakes. *J. Geophys. Res. 111*, B06304. https://doi.org/10.1029/2005JB004001.

Wen, R. Z., Wang, H. W., and Ren, Y. (2015). Rupture directivity from strong-motion recordings of the 2013 Lushan aftershocks. *Bull. Seismol. Soc. Am., 105(6)*, 3068-3082. https://doi.org/10.1785/0120150100.

Wang, H., Ren, Y., Wen, R., and Xu, P. (2019). Breakdown of Earthquake Self-Similar Scaling and Source Rupture Directivity in the 2016-2017 Central Italy Seismic Sequence. *J. Geophys. Res. Solid Earth*, *124*, 3898-3917. https://doi.org/10.1029/ 2018JB016543.

Yamada, T., Mori, J. J., Ide, S., Kawakata, H., Iio, Y., and Ogasawara, H. (2005). Radiation efficiency and apparent stress of small earthquakes in a South African gold mine. *J. Geophys. Res*, *110*, B01305. https://doi.org/10.1029/2004JB003221.

Yin, J., Li, Z., and Denolle, M. A. (2021). Source Time Function Clustering Reveals Patterns in Earthquake Dynamics. *Seismol. Res. Lett. 92*, 2343-2353. https://doi.org/10.1785/ 0220200403.

Yoshida, K. (2019). Prevalence of asymmetrical rupture in small earthquakes and its effect on the estimation of stress drop: a systematic investigation in inland Japan. *Geosci. Lett. 6*, 16. https://doi.org/10.1186/s40562-019-0145.

Figure 1. a) Map of the coverage by ray-paths (lines) connecting events (yellow circles) and stations (red triangles). Red box indicates the study area; b) Plot magnitude-distance from the epicenter. If the Joyner-Boore distance is not available, we use the epicentral distance.

Figure 2. Source areas (with blue dashed boxes) and Mt. Sibillini thrust (with red dashed lines) in a zoomed view with respect to the one shown in Fig. 1a. From South to North: Cluster #1 (main event: L'Aquila 06/04/2009 - 01:32 UTC), #2 (main event: Amatrice 24/08/2016 - 01:36 UTC and Norcia 30/10/2016 06:40 UTC) and #3 (main event: Muccia 10/04/2018 - 03:11 UTC). Red stars represent the mainshocks, while yellow circles are the other events with M > 3.2.

Figure 3. Spatial distribution of the PGA residuals δW_0 for the a) M4 event of 30 October 2016 at 11:58:17, and b) M4 event of 31 October 2016 at 07:05:44. Yellow stars are the epicenters, while reverse triangles represent the stations. Blue/red colors indicate negative/positive residual values (under/over-estimation). The labeled stations are used for illustration of the frequency dependence of the residuals in Fig. 4. Locations in the four quadrants around the epicenter are highlighted. c)-d) Aleatory residuals δW_0 as a function of θ for the same events in a) and b), respectively.

Figure 4. Trend of δW_0 vs frequency for the 4 stations shown in Figure 3, for a) the M4 event of 30 October 2016 at 11:58:17, and b) the M4 event of 31 October 2016 at 07:05:44.

Figure 5. Azimuthal variation of the aleatory residuals for a Mw 4.0 event of 30 October 2016, 11:58:17 at a) f=1 Hz, c) f=5 Hz, e) f=10 Hz. In black, fit with cosinusoidal function (Case I), in red fit with k = 1 and α= 0.7 (Case II), in blue α = 0.5 and k = 0.85 (Case III), while with the green curve the fit is estimated with an optimization algorithm (in this case, k tends to 1 and α is close to 0.5 - Case IV).

Figure 6. Directivity amplitude (top); direction of rupture propagation (middle); coefficient of determination (bottom) plotted versus frequency. The black curve represents the fitting results with the cosine model, the blue curve with the C_d model. Red lines represent the minimum and maximum frequency within which the *proxy* R^2 is larger than 0.5. a) M4 event of 30 October 2016 at 11:58:17; b) M4 event of 31 October 2016 at 07:05:44.

Figure 7. Directivity frequency bandwidth of the events in the magnitude range from 3.7 to 4.0. Each frequency interval of the bandwidth (on x-axis) is colored according to the value of amplitude n. Since the frequency range is logarithmically equispaced, at the top part of x-axis is shown the log2 frequency, and the corresponding frequency content is shown at the bottom part of x-axis.

Figure 8. a) Number of directive events (yellow) compared to the event distributions (red) of the study dataset, grouped in magnitude bins. b) Percentage of the events with R^2 > 0.5 out of the total number of events as a function of frequency for different magnitude intervals (see legend).

Figure 9. Minimum frequency (log2 f_{min}, red dots) and maximum frequency (log2 f_{max}, green dots) where the directivity effect is present plotted as a function of magnitude. Blue stars are the corner frequency from Bindi et al. (2018) and magenta squares are the values obtained by multiplying the minimum frequency by a factor of 5. Solid lines represent the median values over magnitude bin width.

Figure 10. a) Median and b) maximum value of the exponent n for the events with directivity among all observed frequency ranges.

Figure 11. Frequency bandwidth against values n_{med}. The size of the circles is proportional to the magnitude; black dashed line represents the fit curve. The yellow box shows the empirical linear relation between the frequency bandwidth and n_{med}.

Figure 12. Median value of the direction of rupture propagation for all the directive events.

Figure 13. a) Comparison between the median of the direction of rupture propagation θ_0 and the closest strike inferred by Herrmann et al. (2021) for the analyzed directive events. The size of red dots is proportional to the moment magnitude, while the red dashed line represents the bisector at 45°.
b) Direction of rupture propagation for the 10 most directive events according to the work of Wang et al. (2019). Blue points are the angles θ_0 determined by Wang et al. (2019) and red ones are those estimates in this research. Error bars express the mean $\pm$ 1 standard deviation within the frequency band where we observe directivity.

Figure 14. a) Map of the events (yellow dots, size is proportional to the magnitude) divided in a cluster at the North and at the South with respect to the Mt. Sibillini thrust (red line). b) Distribution of the median values of the direction of rupture propagation for the two clusters: bluish colors for the northern cluster, reddish colors for the southern cluster. c) Events with directivity in the cluster North and d) in the cluster South. For the cluster North, events with direction of rupture propagation towards North (270-90°) are in light blue while the ones with direction towards South (270-90°) are in dark blue. For the cluster South, events towards North are in light red and towards South in dark red. Yellow stars are the mainshocks for the analyzed earthquakes.

Figure 15. Relation between minimum frequency f_{min} and bandwidth, defined as log2 $\frac{f_{max}}{f_{min}}$. The color of the circles represent the value of n_{med}. Three domains are shown in the graph, defined according to the 75th percentile. With crosses, it shows how we can classify an event with Mw 4.6, where $f_{min} = f_c$, equal at about 1 Hz (see Fig. 9). Light-yellow cross shows an event with weak directivity (input value $n_{med} = 0.55$) where log2 $\frac{f_{max}}{f_{min}}$ is equal to 1.36 octaves; red cross represent the case with high directivity (input value $n_{med} = 1.55$) and log2 $\frac{f_{max}}{f_{min}}$ equal to 4.1 octaves. The large grey triangle with mesh net in the upper right portion of the graph defines the limit of the existence domain of our frequency interval, where $f_{max} = 25$ Hz.

Table 1. Values of amplitude (A or n), azimuth θ_0, coefficient of determination R^2 and standard deviation σ for different cases reported in Fig. 5. a) f=1 Hz, b) f=5 Hz, c) f=10 Hz.

a)

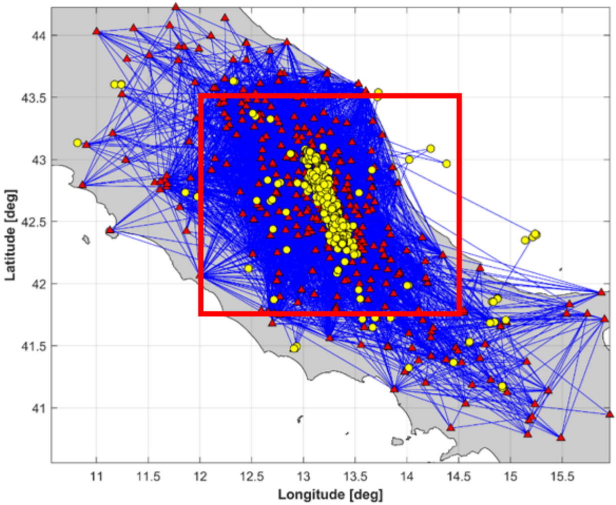
Latitude [deg]
44
43.5
43
42.5
42
41.5
41
Longitude [deg]
11
11.5
12
12.5
13
13.5
14
14.5
15
15.5

b)

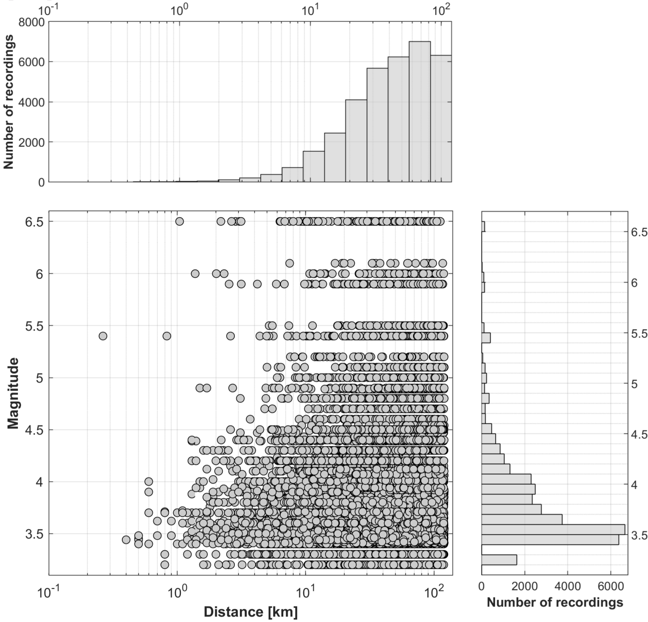
Number of recordings
8000
6000
4000
2000
0
10^{-1}
10^{0}
10^{1}
10^{2}
Magnitude
6.5
6
5.5
5
4.5
4
3.5
Distance [km]
0
2000
4000
6000
Number of recordings

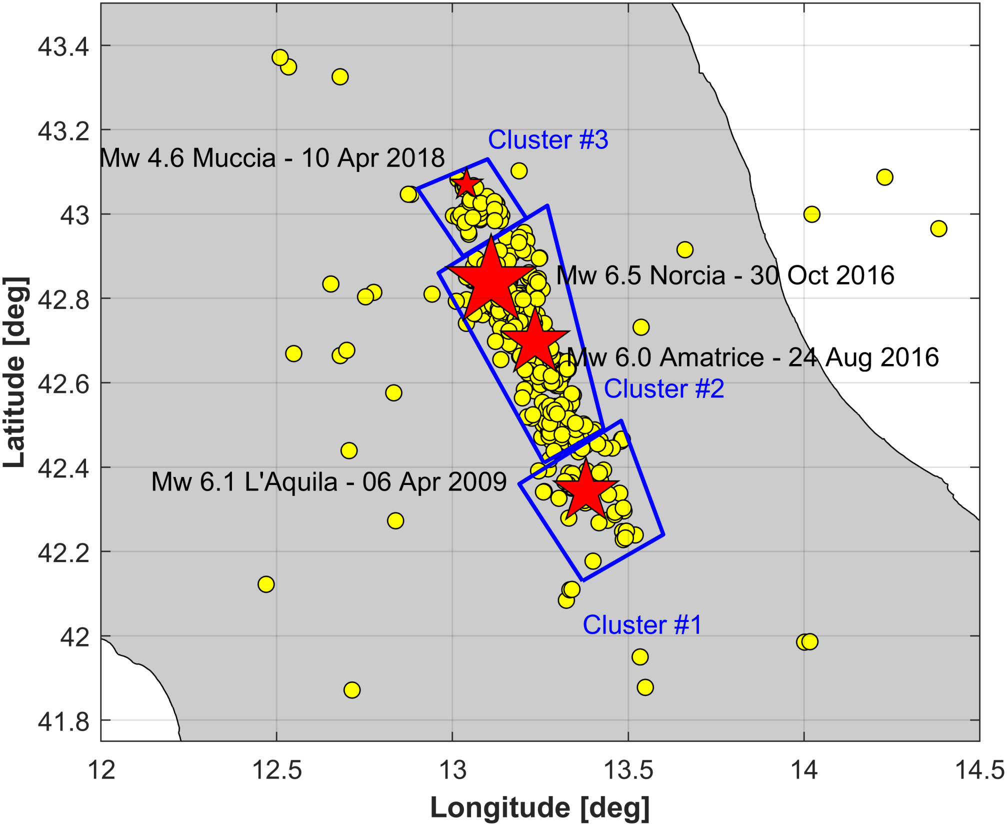
Cluster #3
Mw 4.6 Muccia - 10 Apr 2018
Mw 6.5 Norcia - 30 Oct 2016
Mw 6.0 Amatrice - 24 Aug 2016
Cluster #2
Mw 6.1 L'Aquila - 06 Apr 2009
Cluster #1
43.4
43.2
43
42.8
42.6
42.4
42.2
42
41.8
12
12.5
13
13.5
14
14.5
Latitude [deg]
Longitude [deg]

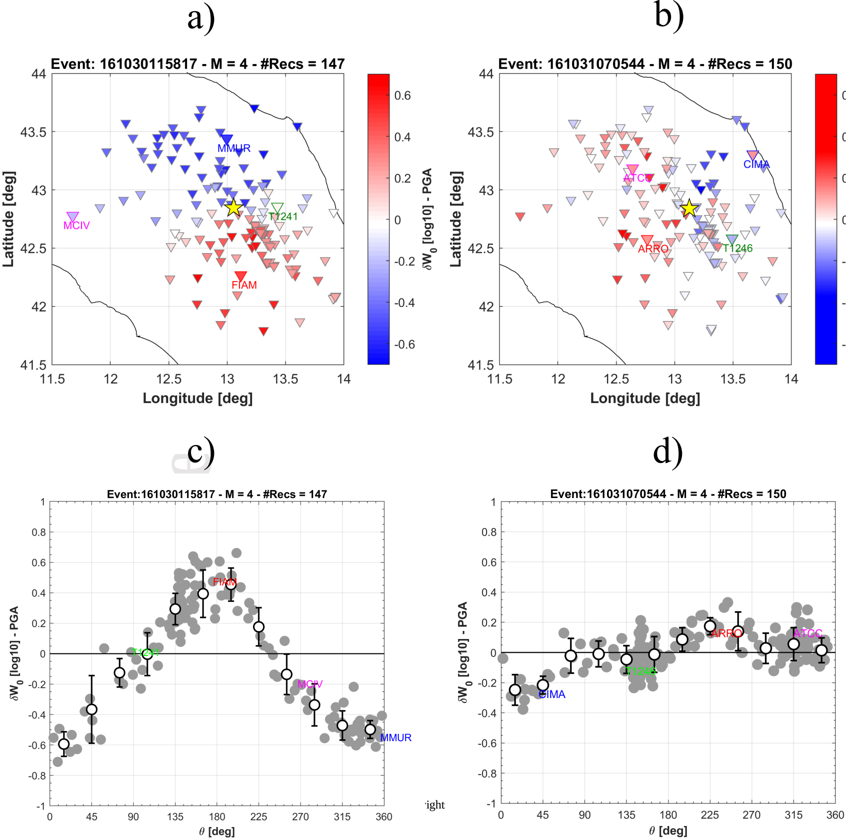
a)
b)
Event: 161030115817 - M = 4 - #Recs = 147
Event: 161031070544 - M = 4 - #Recs = 150
Latitude [deg]
Longitude [deg]
44
43.5
43
42.5
42
41.5
11.5
12
12.5
13
13.5
14
MMUR
MCIV
T1241
FIAM
CIMA
ATCC
ARRO
T1246
0.6
0.4
0.2
0
-0.2
-0.4
-0.6
δW_0 [log10] - PGA
c)
d)
Event:161030115817 - M = 4 - #Recs = 147
Event:161031070544 - M = 4 - #Recs = 150
δW_0 [log10] - PGA
θ [deg]
1
0.8
0.6
0.4
0.2
0
-0.2
-0.4
-0.6
-0.8
-1
0
45
90
135
180
225
270
315
360
ight

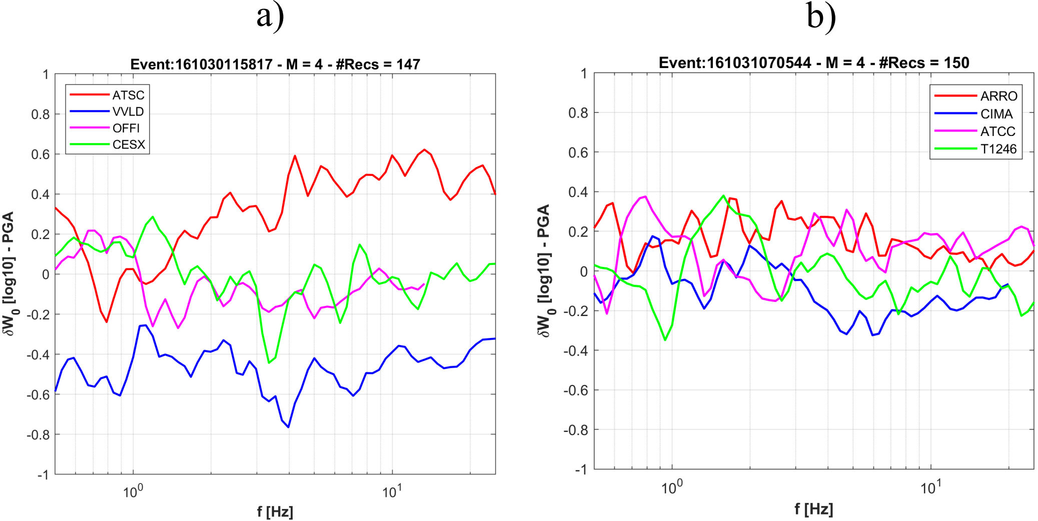
a)
Event:161030115817 - M = 4 - #Recs = 147
ATSC
VVLD
OFFI
CESX
δW_0 [log10] - PGA
1
0.8
0.6
0.4
0.2
0
-0.2
-0.4
-0.6
-0.8
-1
10^0
10^1
f [Hz]
b)
Event:161031070544 - M = 4 - #Recs = 150
ARRO
CIMA
ATCC
T1246
δW_0 [log10] - PGA
1
0.8
0.6
0.4
0.2
0
-0.2
-0.4
-0.6
-0.8
-1
10^0
10^1
f [Hz]

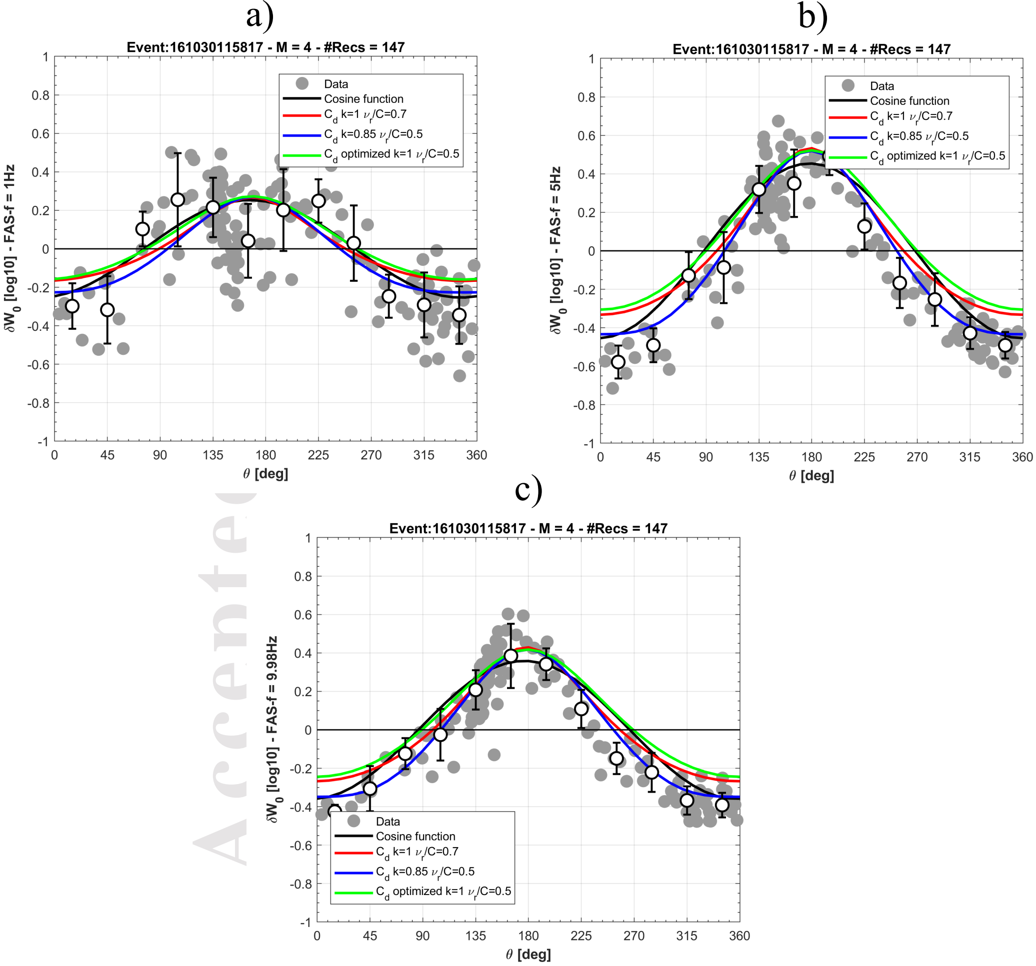
a)
Event:161030115817 - M = 4 - #Recs = 147
δW$_0$ [log10] - FAS-f = 1Hz
θ [deg]
Data
Cosine function
C$_d$ k=1 ν$_r$/C=0.7
C$_d$ k=0.85 ν$_r$/C=0.5
C$_d$ optimized k=1 ν$_r$/C=0.5
1
0.8
0.6
0.4
0.2
0
-0.2
-0.4
-0.6
-0.8
-1
0
45
90
135
180
225
270
315
360
b)
Event:161030115817 - M = 4 - #Recs = 147
δW$_0$ [log10] - FAS-f = 5Hz
θ [deg]
Data
Cosine function
C$_d$ k=1 ν$_r$/C=0.7
C$_d$ k=0.85 ν$_r$/C=0.5
C$_d$ optimized k=1 ν$_r$/C=0.5
c)
Event:161030115817 - M = 4 - #Recs = 147
δW$_0$ [log10] - FAS-f = 9.98Hz
θ [deg]
Data
Cosine function
C$_d$ k=1 ν$_r$/C=0.7
C$_d$ k=0.85 ν$_r$/C=0.5
C$_d$ optimized k=1 ν$_r$/C=0.5

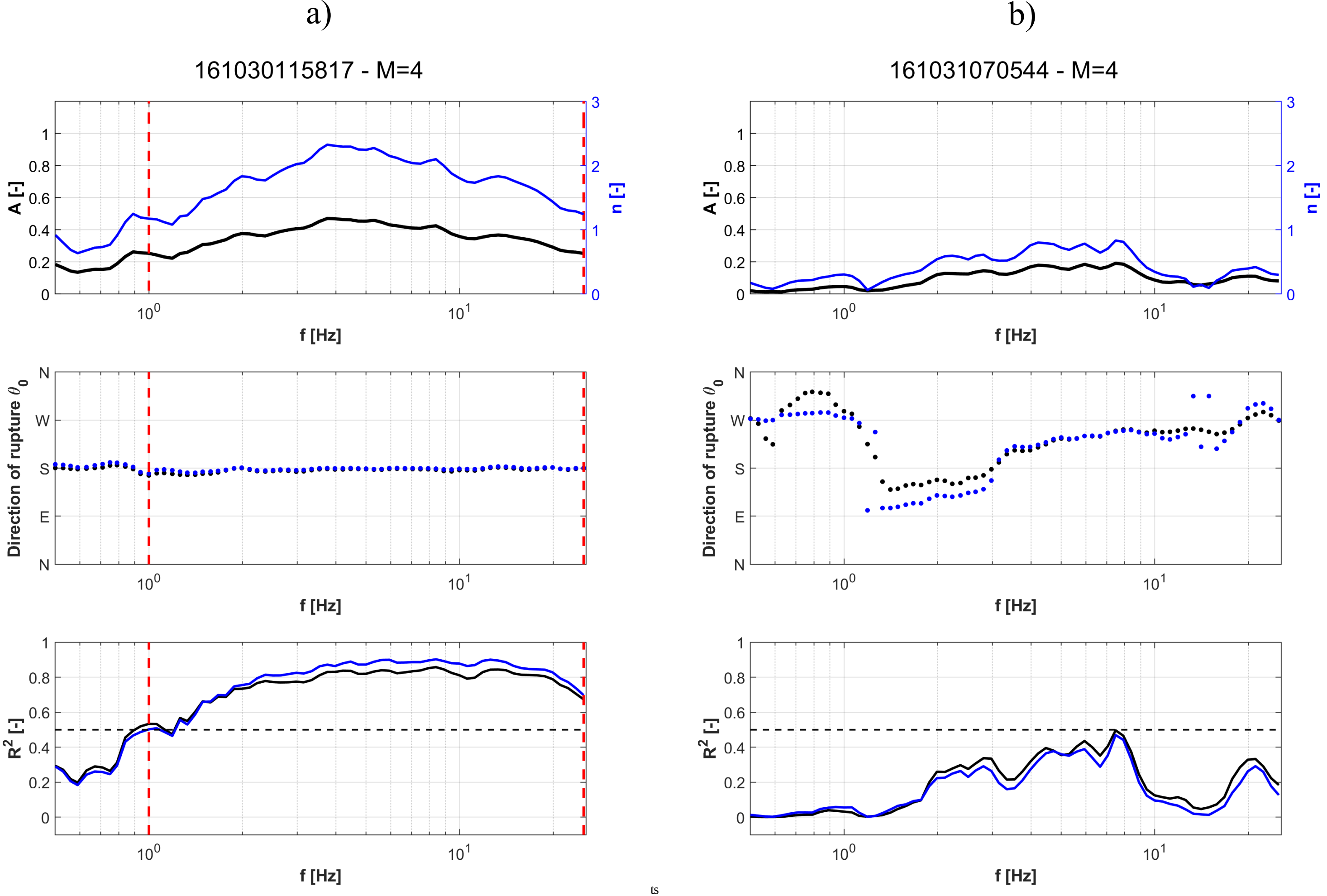
a)
b)
161030115817 - M=4
161031070544 - M=4
A [-]
n [-]
0
0.2
0.4
0.6
0.8
1
0
1
2
3
f [Hz]
10^0
10^1
Direction of rupture θ_0
N
W
S
E
N
R^2 [-]

ts

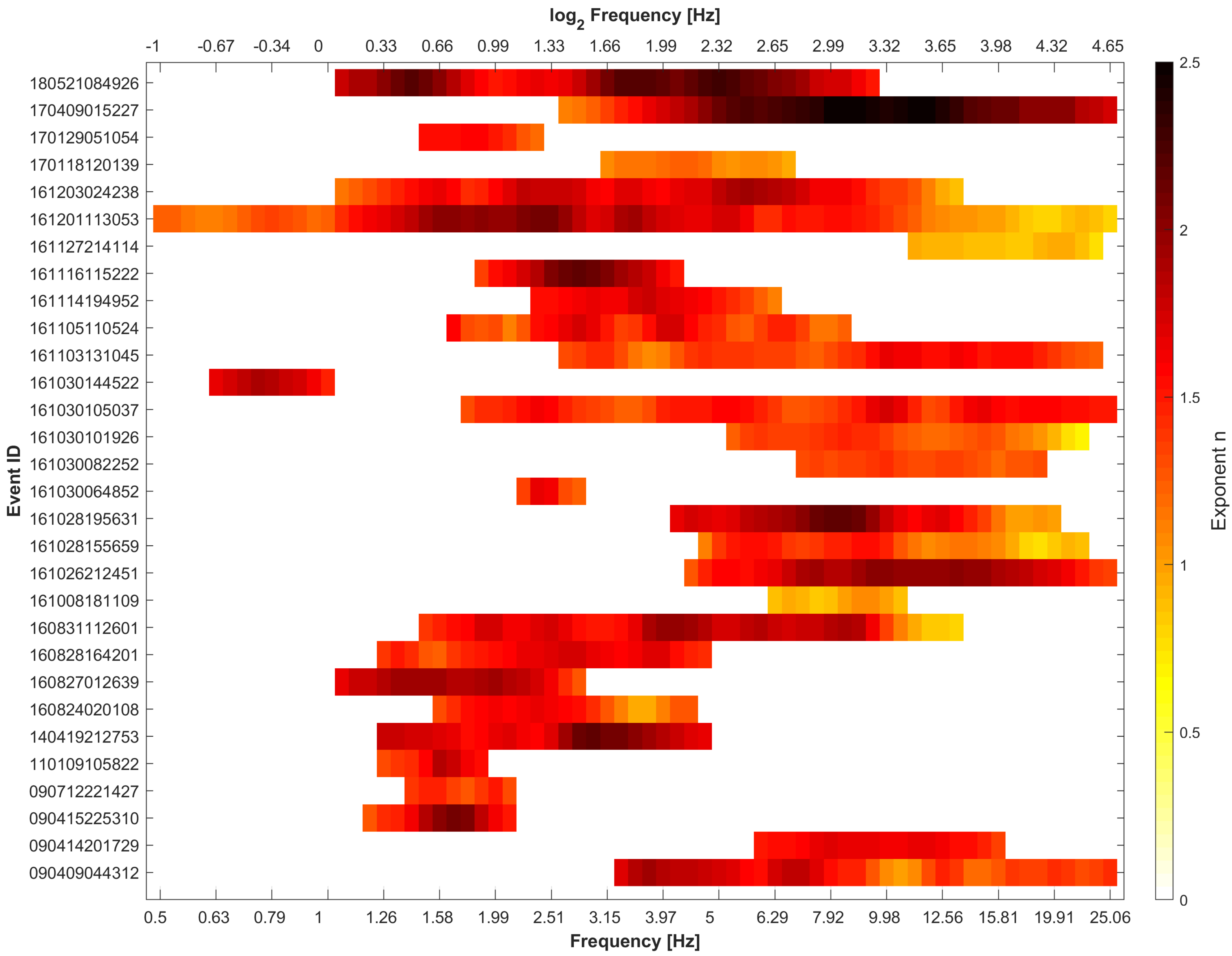
log2 Frequency [Hz]
-1
-0.67
-0.34
0
0.33
0.66
0.99
1.33
1.66
1.99
2.32
2.65
2.99
3.32
3.65
3.98
4.32
4.65
Event ID
180521084926
170409015227
170129051054
170118120139
161203024238
161201113053
161127214114
161116115222
161114194952
161105110524
161103131045
161030144522
161030105037
161030101926
161030082252
161030064852
161028195631
161028155659
161026212451
161008181109
160831112601
160828164201
160827012639
160824020108
140419212753
110109105822
090712221427
090415225310
090414201729
090409044312
0.5
0.63
0.79
1
1.26
1.58
1.99
2.51
3.15
3.97
5
6.29
7.92
9.98
12.56
15.81
19.91
25.06
Frequency [Hz]
2.5
2
1.5
1
0.5
0
Exponent n

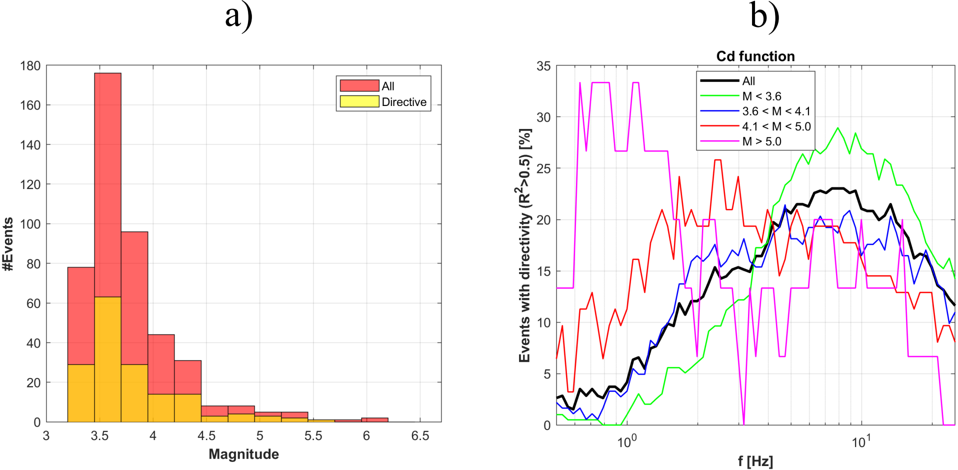
a)
b)
180
160
140
120
100
80
60
40
20
0
#Events
3
3.5
4
4.5
5
5.5
6
6.5
Magnitude
All
Directive
Cd function
35
30
25
20
15
10
5
0
Events with directivity (R^2>0.5) [%]
10^0
10^1
f [Hz]
All
M < 3.6
3.6 < M < 4.1
4.1 < M < 5.0
M > 5.0

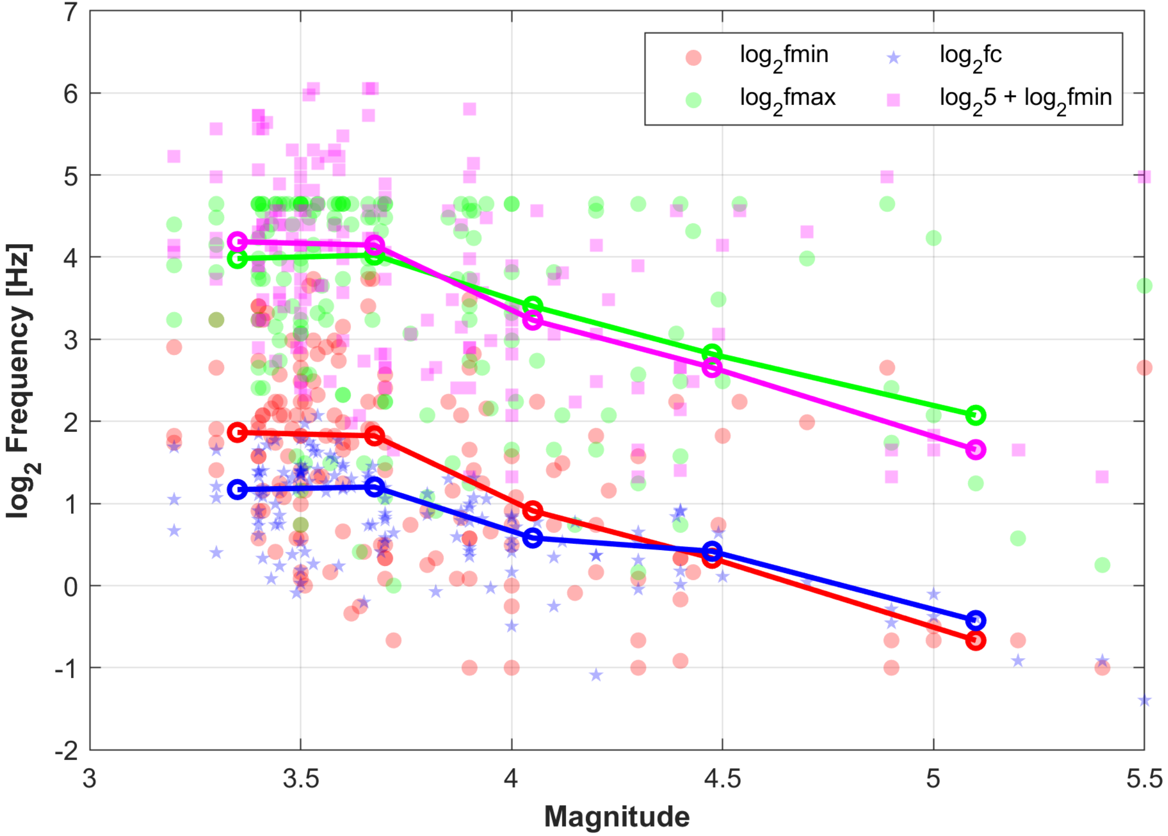
log$_2$fmin
log$_2$fc
log$_2$fmax
log$_2$5 + log$_2$fmin
log$_2$ Frequency [Hz]
Magnitude
7
6
5
4
3
2
1
0
-1
-2
3
3.5
4
4.5
5
5.5

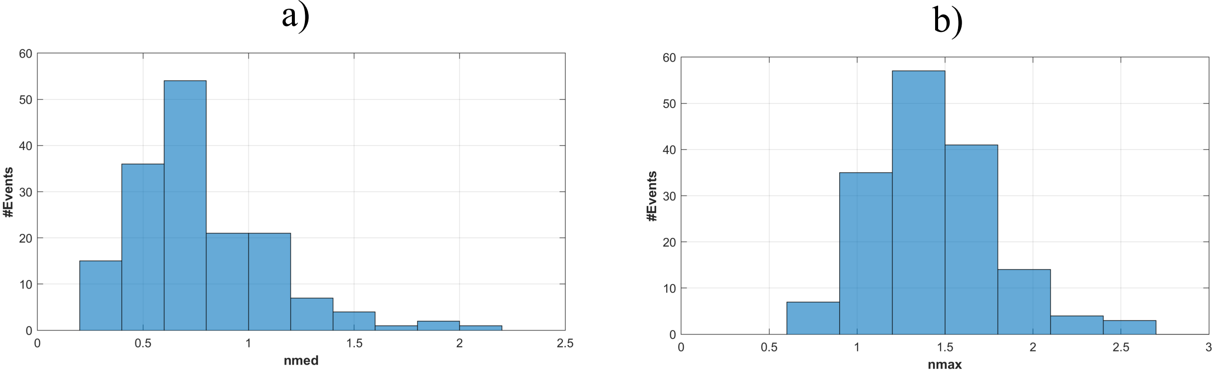
a)
60
50
40
30
20
10
0
#Events
0
0.5
1
1.5
2
2.5
nmed
b)
60
50
40
30
20
10
0
#Events
0
0.5
1
1.5
2
2.5
3
nmax

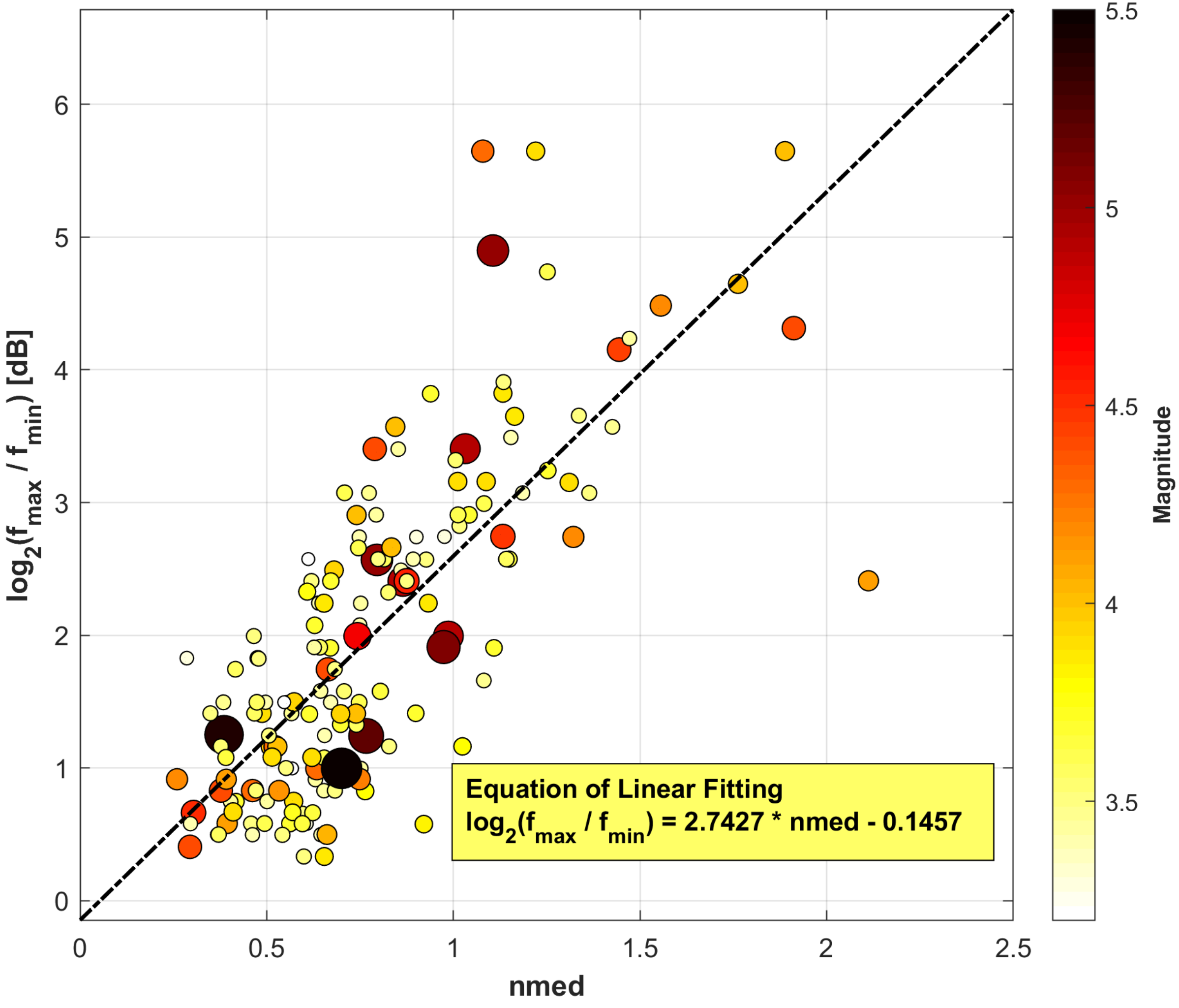

log$_2$(f$_{max}$ / f$_{min}$) [dB]
0
1
2
3
4
5
6
0
0.5
1
1.5
2
2.5
nmed
5.5
5
4.5
4
3.5
Magnitude
Equation of Linear Fitting
log$_2$(f$_{max}$ / f$_{min}$) = 2.7427 * nmed - 0.1457

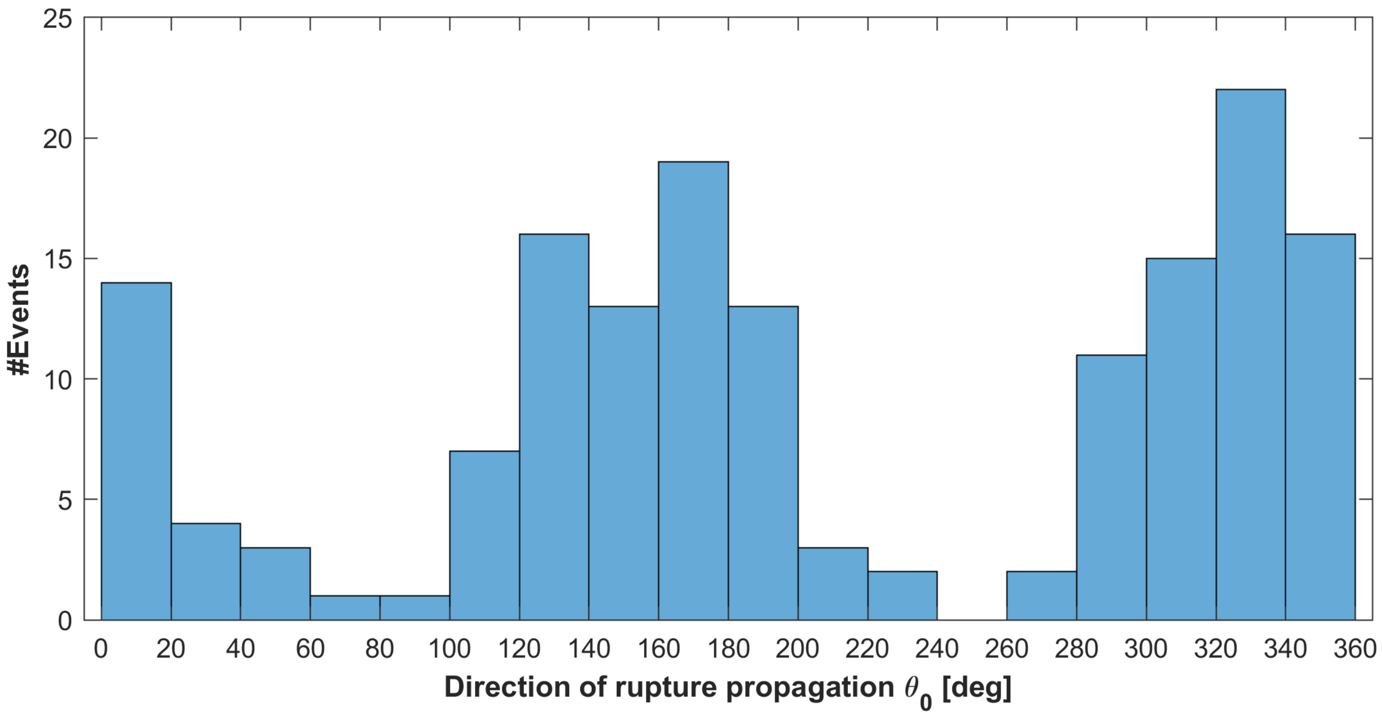
#Events
0
5
10
15
20
25
0
20
40
60
80
100
120
140
160
180
200
220
240
260
280
300
320
340
360
Direction of rupture propagation θ_0 [deg]

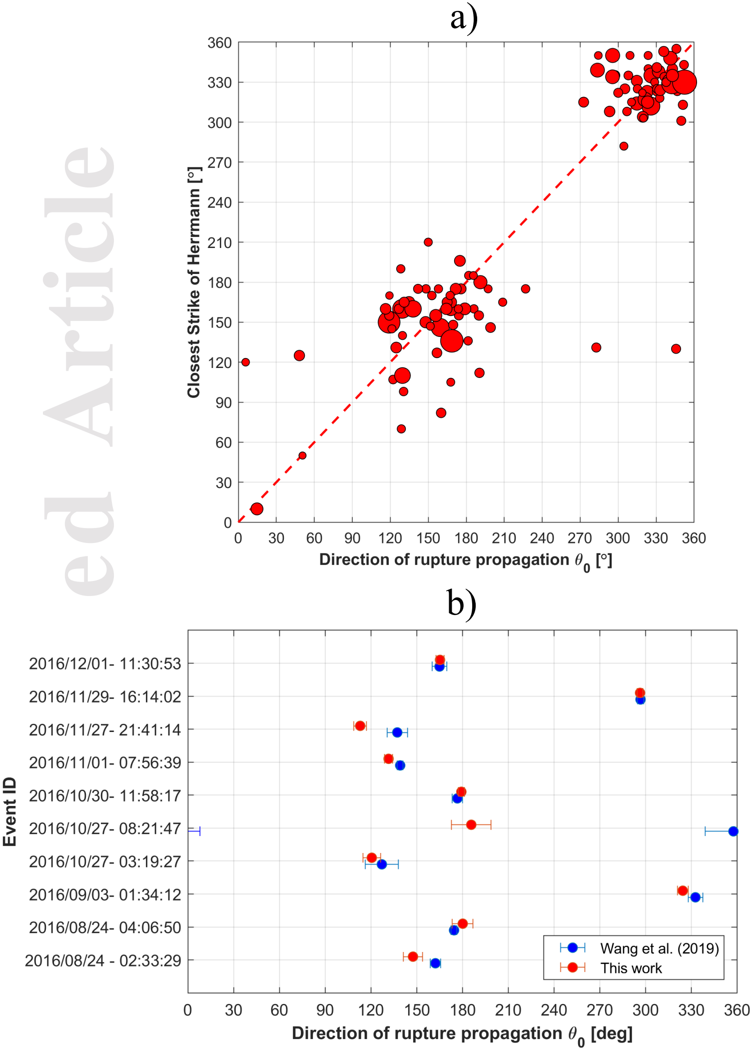
a)
Closest Strike of Herrmann [°]
0
30
60
90
120
150
180
210
240
270
300
330
360
Direction of rupture propagation θ_0 [°]
b)
Event ID
2016/12/01- 11:30:53
2016/11/29- 16:14:02
2016/11/27- 21:41:14
2016/11/01- 07:56:39
2016/10/30- 11:58:17
2016/10/27- 08:21:47
2016/10/27- 03:19:27
2016/09/03- 01:34:12
2016/08/24- 04:06:50
2016/08/24 - 02:33:29
Wang et al. (2019)
This work
Direction of rupture propagation θ_0 [deg]

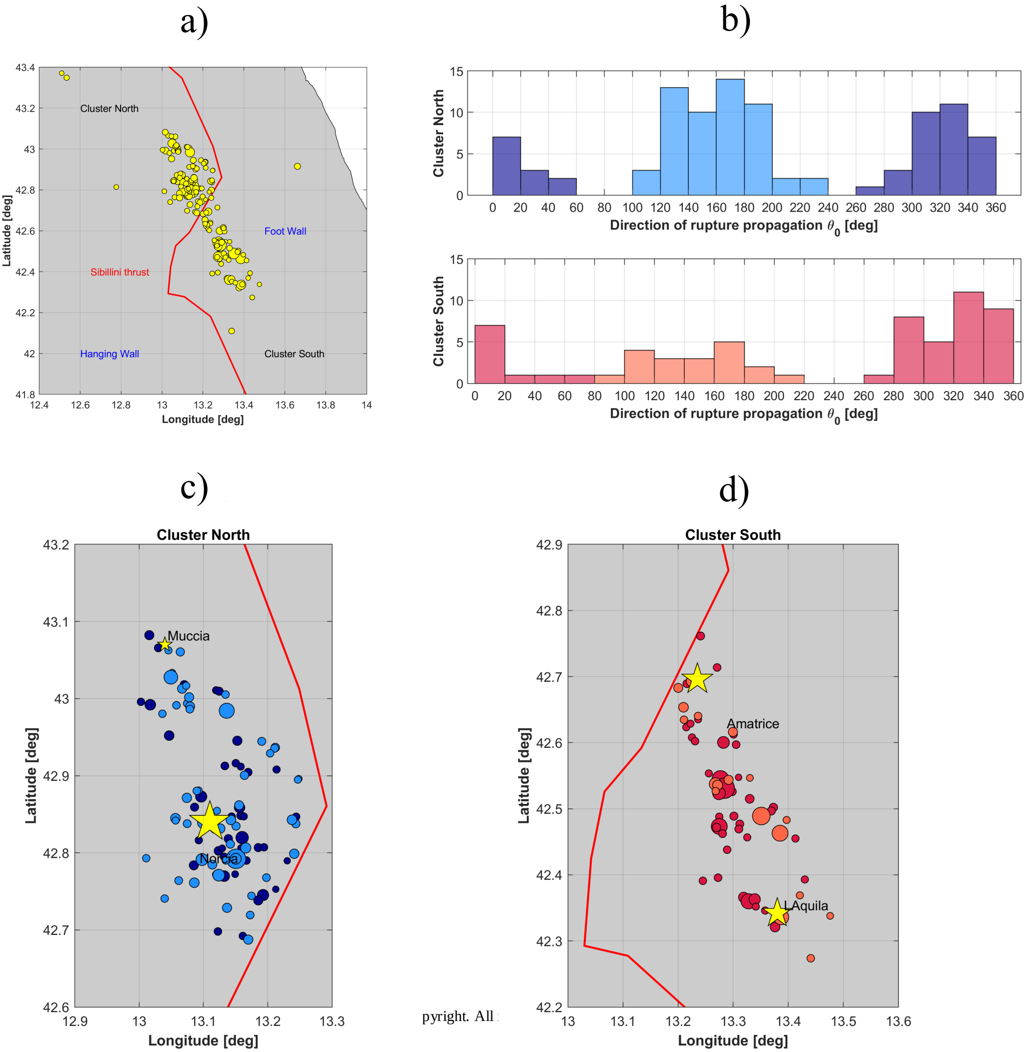
a)
b)
c)
d)
Cluster North
Cluster South
Sibillini thrust
Foot Wall
Hanging Wall
Latitude [deg]
Longitude [deg]
43.4
43.2
43
42.8
42.6
42.4
42.2
42
41.8
12.4
12.6
12.8
13
13.2
13.4
13.6
13.8
14
Cluster North
Cluster South
15
10
5
0
0
20
40
60
80
100
120
140
160
180
200
220
240
260
280
300
320
340
360
Direction of rupture propagation θ_0 [deg]
Direction of rupture propagation θ_0 [deg]
Cluster North
Muccia
Norcia
Latitude [deg]
Longitude [deg]
43.2
43.1
43
42.9
42.8
42.7
42.6
12.9
13
13.1
13.2
13.3
Cluster South
Amatrice
LAquila
Latitude [deg]
Longitude [deg]
42.9
42.8
42.7
42.6
42.5
42.4
42.3
42.2
13
13.1
13.2
13.3
13.4
13.5
13.6

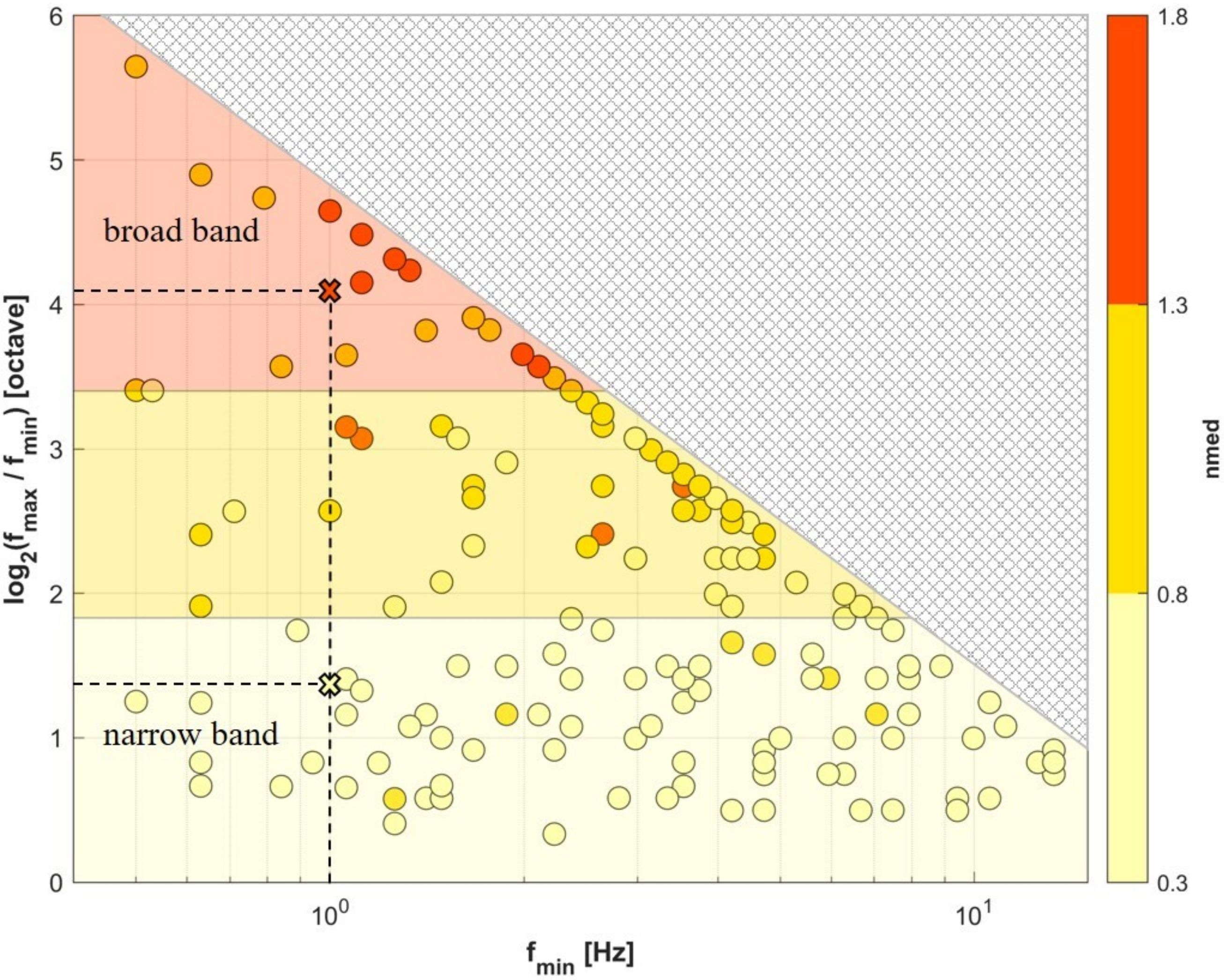
broad band
narrow band
log$_2$(f$_{max}$ / f$_{min}$) [octave]
f$_{min}$ [Hz]
0
1
2
3
4
5
6
10^0
10^1
nmed
1.8
1.3
0.8
0.3

a)

Case	A or n	θ_0 (°)	R^2	σ
I	0.2534	166.34	0.5338	0.1884
II	0.5770	168.52	0.4436	0.2050
III	1.1736	169.74	0.5024	0.1988
IV	0.9062	168.41	0.5186	0.1996

b)

Case	A or n	θ_0 (°)	R^2	σ
I	0.4537	178.17	0.8200	0.1410
II	1.1488	178.66	0.8011	0.1415
III	2.2469	179.06	0.8732	0.1289
IV	1.7347	179.87	0.8108	0.1452

c)

Case	A or n	θ_0 (°)	R^2	σ
I	0.3586	176.26	0.8118	0.1169
II	0.9248	178.19	0.8123	0.1079
III	1.8064	178.87	0.8786	0.1007
IV	1.3872	179.17	0.8200	0.1154

Journal of Geophysical Research: Solid Earth

Supporting Information for

Empirical Evidence of Frequency-Dependent Directivity Effects from Small-to-Moderate Normal Fault Earthquakes in Central Italy

Leonardo Colavitti[1], Giovanni Lanzano[1], Sara Sgobba[1], Francesca Pacor[1], Frantisek Gallovic[2]

1 National Institute of Geophysics and Volcanology, Section of Seismology applied to Engineering, Milano, Italy

2 Charles University, Faculty of Mathematics and Physics, Department of Geophysics, Prague, Czech Republic

Contents of this file

Figures $\mathbf{S_1}$ to $\mathbf{S_{10}}$

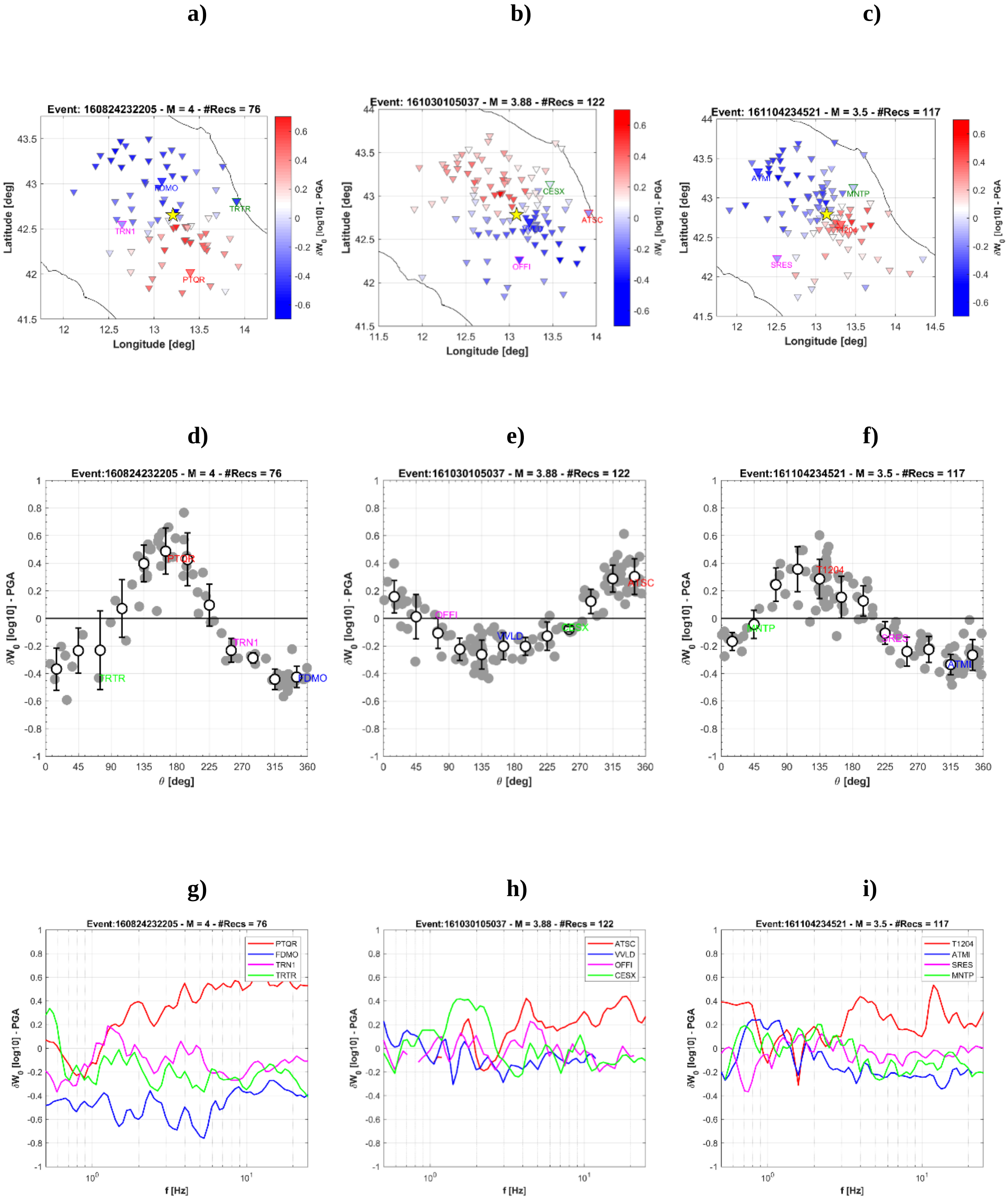

Figure S$_1$. a-b-c) Map of the stations (shown with reverse triangles) with the values of W_0 for the PGA (in blue-white-red scale) for three events, from left to right: M4 of 24 August 2016 at 23:22:05, M3.88 of 30 October 2016 at 10:50:37, M3.5 of 04 November 2016 at 23:45:21. Yellow stars represent the epicenters.
d-e-f) Patterns of the aleatory PGA residuals W_0 as a function of azimuth angle θ.
g-h-i) Trend representation of W_0 for 4 positions: directive (red), neutrals (green and magenta) and anti-directive (blue) in the computed frequency range from 0.5 to 25 Hz.

a)

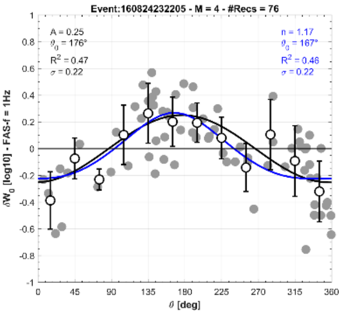
Event:160824232205 - M = 4 - #Recs = 76
A = 0.25
ϑ_0 = 176°
R^2 = 0.47
σ = 0.22
n = 1.17
ϑ_0 = 167°
R^2 = 0.46
σ = 0.22
δW_0 [log10] - FAS-f = 1Hz
θ [deg]

b)

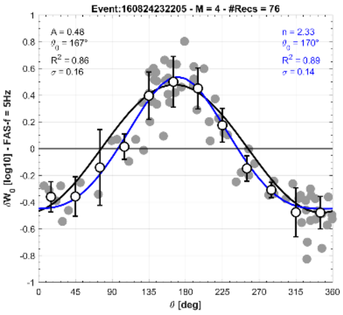
Event:160824232205 - M = 4 - #Recs = 76
A = 0.48
ϑ_0 = 167°
R^2 = 0.86
σ = 0.16
n = 2.33
ϑ_0 = 170°
R^2 = 0.89
σ = 0.14
δW_0 [log10] - FAS-f = 5Hz
θ [deg]

c)

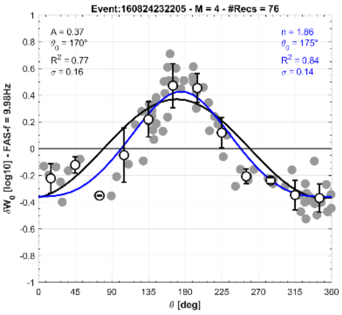
Event:160824232205 - M = 4 - #Recs = 76
A = 0.37
ϑ_0 = 170°
R^2 = 0.77
σ = 0.16
n = 1.86
ϑ_0 = 175°
R^2 = 0.84
σ = 0.14
δW_0 [log10] - FAS-f = 9.98Hz
θ [deg]

d)

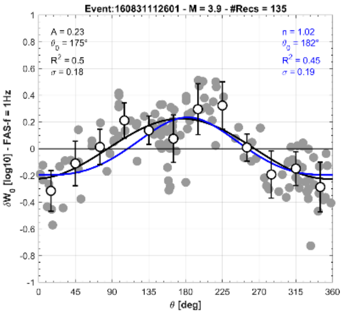
Event:160831112601 - M = 3.9 - #Recs = 135
A = 0.23
ϑ_0 = 175°
R^2 = 0.5
σ = 0.18
n = 1.02
ϑ_0 = 182°
R^2 = 0.45
σ = 0.19
δW_0 [log10] - FAS-f = 1Hz
θ [deg]

e)

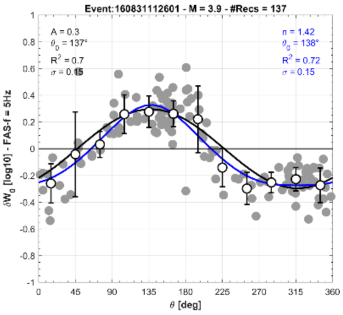
Event:160831112601 - M = 3.9 - #Recs = 137
A = 0.3
ϑ_0 = 137°
R^2 = 0.7
σ = 0.15
n = 1.42
ϑ_0 = 138°
R^2 = 0.72
σ = 0.15
δW_0 [log10] - FAS-f = 5Hz
θ [deg]

f)

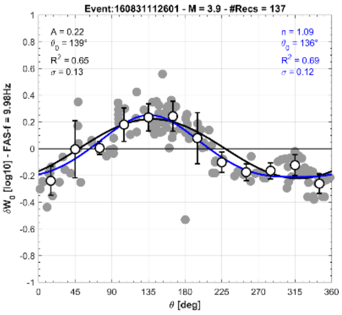
Event:160831112601 - M = 3.9 - #Recs = 137
A = 0.22
ϑ_0 = 139°
R^2 = 0.65
σ = 0.13
n = 1.09
ϑ_0 = 136°
R^2 = 0.69
σ = 0.12
δW_0 [log10] - FAS-f = 9.98Hz
θ [deg]

g)

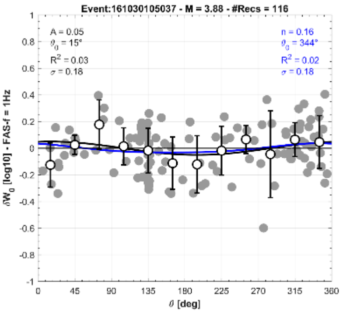
Event:161030105037 - M = 3.88 - #Recs = 116
A = 0.05
ϑ_0 = 15°
R^2 = 0.03
σ = 0.18
n = 0.16
ϑ_0 = 344°
R^2 = 0.02
σ = 0.18
δW_0 [log10] - FAS-f = 1Hz
θ [deg]

h)

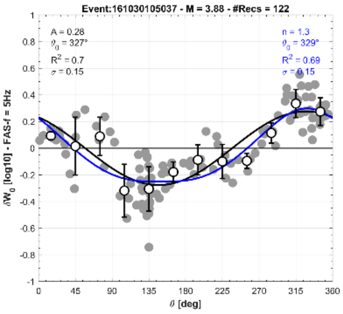
Event:161030105037 - M = 3.88 - #Recs = 122
A = 0.28
ϑ_0 = 327°
R^2 = 0.7
σ = 0.15
n = 1.3
ϑ_0 = 329°
R^2 = 0.69
σ = 0.15
δW_0 [log10] - FAS-f = 5Hz
θ [deg]

i)

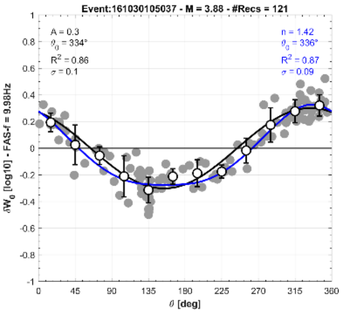
Event:161030105037 - M = 3.88 - #Recs = 121
A = 0.3
ϑ_0 = 334°
R^2 = 0.86
σ = 0.1
n = 1.42
ϑ_0 = 336°
R^2 = 0.87
σ = 0.09
δW_0 [log10] - FAS-f = 9.98Hz
θ [deg]

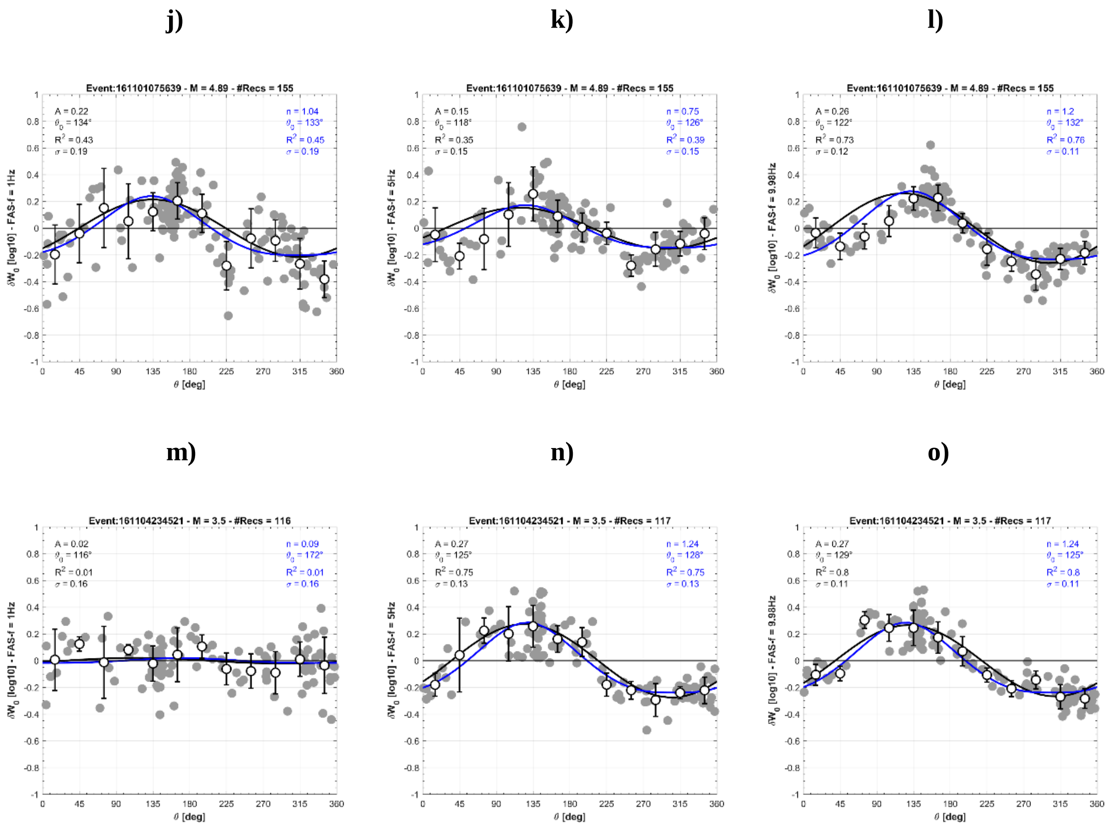

Figure S$_2$. Azimuthal variation of the aleatory residuals fitted with cosine function (black curve and legend) and C_d function (blue curve and legend).
M4 event of 24 August 2016 at 23:22:05: **a)** f=1 Hz, **b)** f=5 Hz, **c)** f=10 Hz.
M 3.9 event of 31 August 2016 at 11:26:01: **d)** f=1 Hz, **e)** f=5 Hz, **f)** f=10 Hz.
M 3.88 event of 30 October 2016 at 10:50:37: **g)** f=1 Hz, **h)** f=5 Hz, **i)** f=10 Hz.
M 4.89 event of 1 November 2016 at 07:56:39: **j)** f= 1 Hz, **k)** f=5 Hz, **l)** f=10 Hz.
M 3.5 event of 4 November 2016 at 23:45:21: **m)** f=1Hz, **n)** f=5 Hz, **o)** f=10 Hz.
Results for C_d function are obtained considering $k = 0.85$ and Mach number $\alpha = 0.5$.

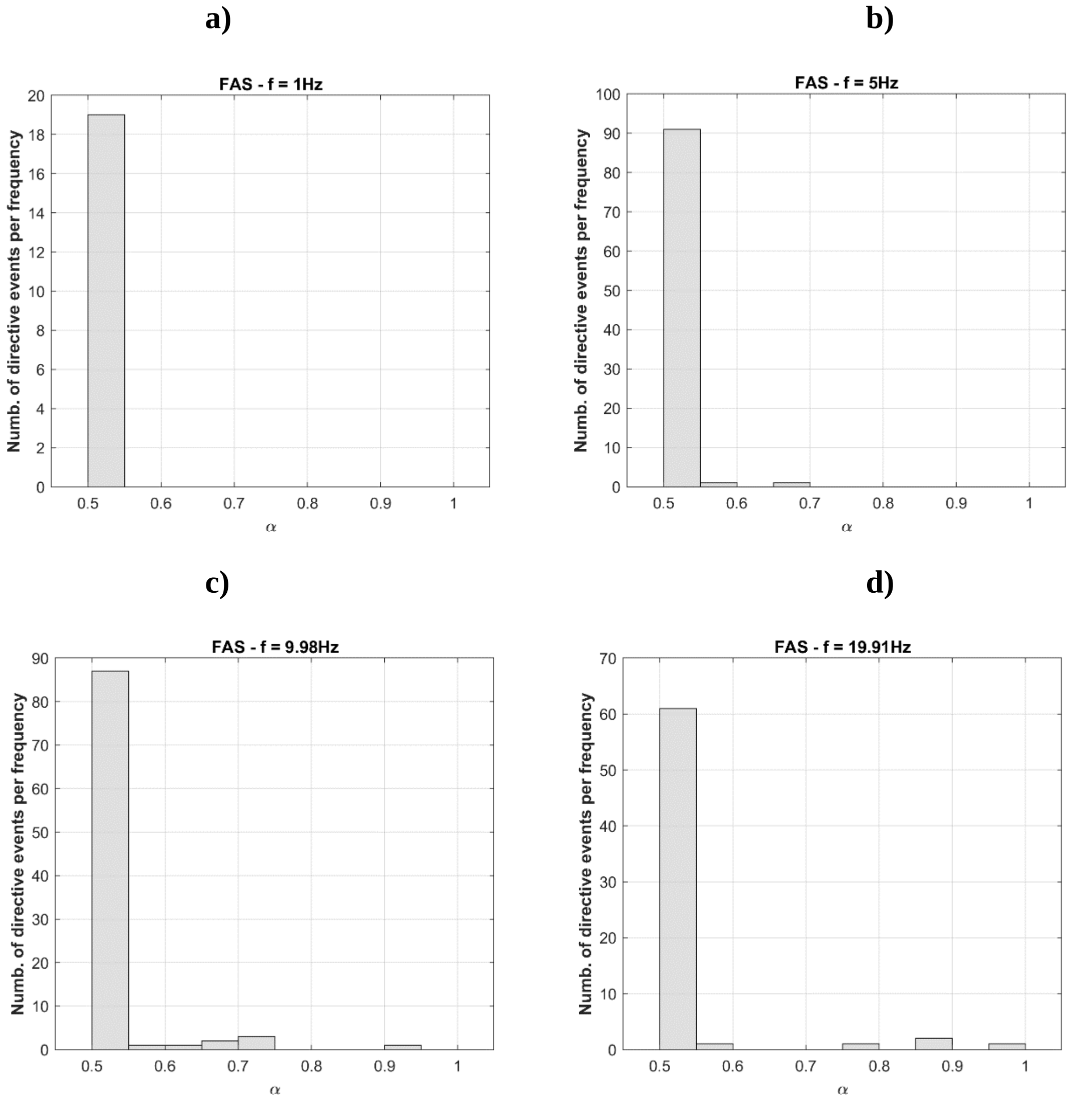

Figure S$_3$. Distribution of α parameter for 1 Hz **a)**, 5 Hz **b)**, 10 Hz **c)** and 20 Hz **d)**. Y-axis represents the number of directive events per frequency; α value is free to vary between 0.5 and 1.

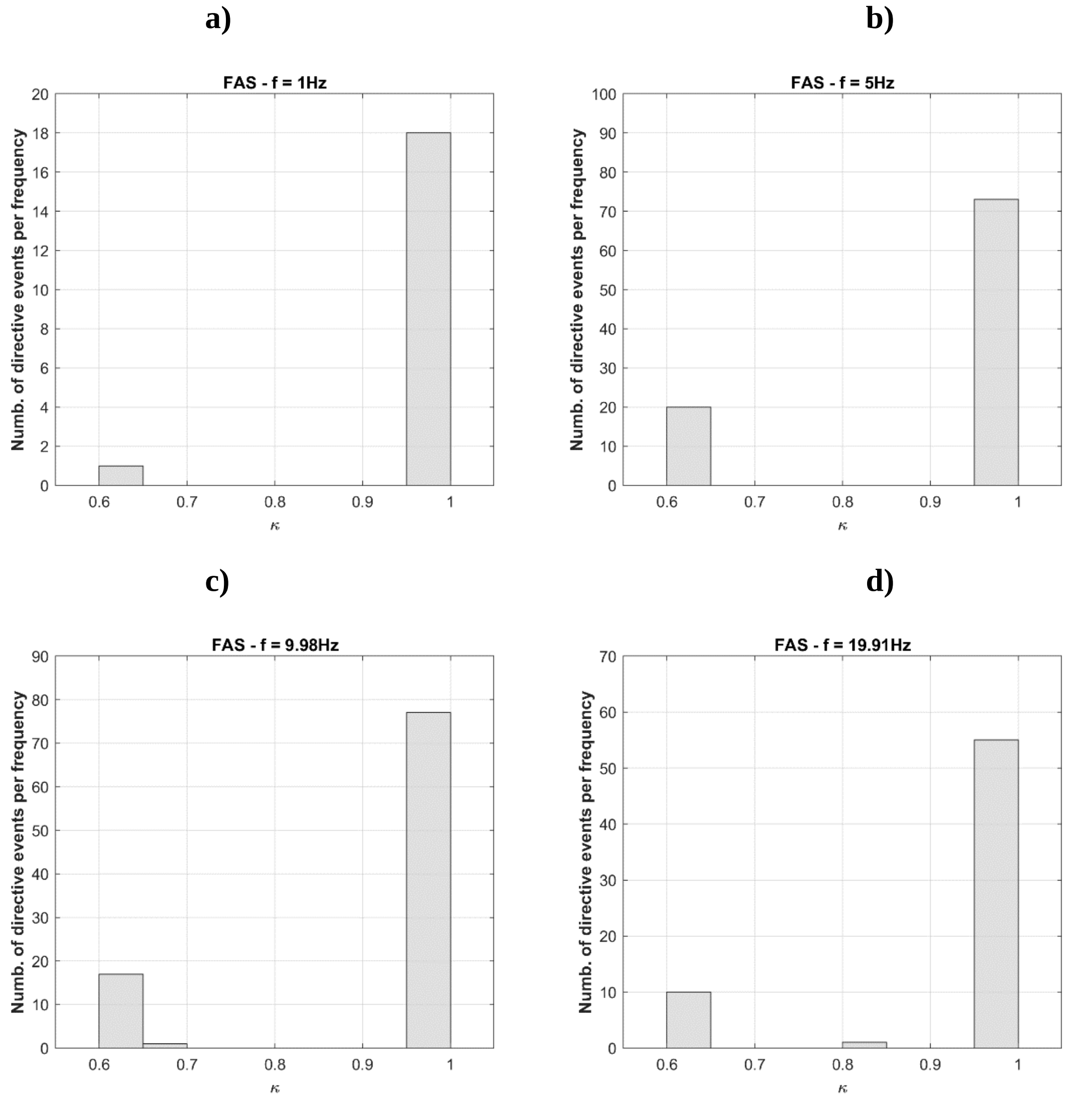

Figure S$_4$. Distribution of k parameter for 1 Hz **a)**, 5 Hz **b)**, 10 Hz **c)** and 20 Hz **d)**. Y-axis represents the number of directive events per frequency; α value is free to vary between 0.5 and 1.

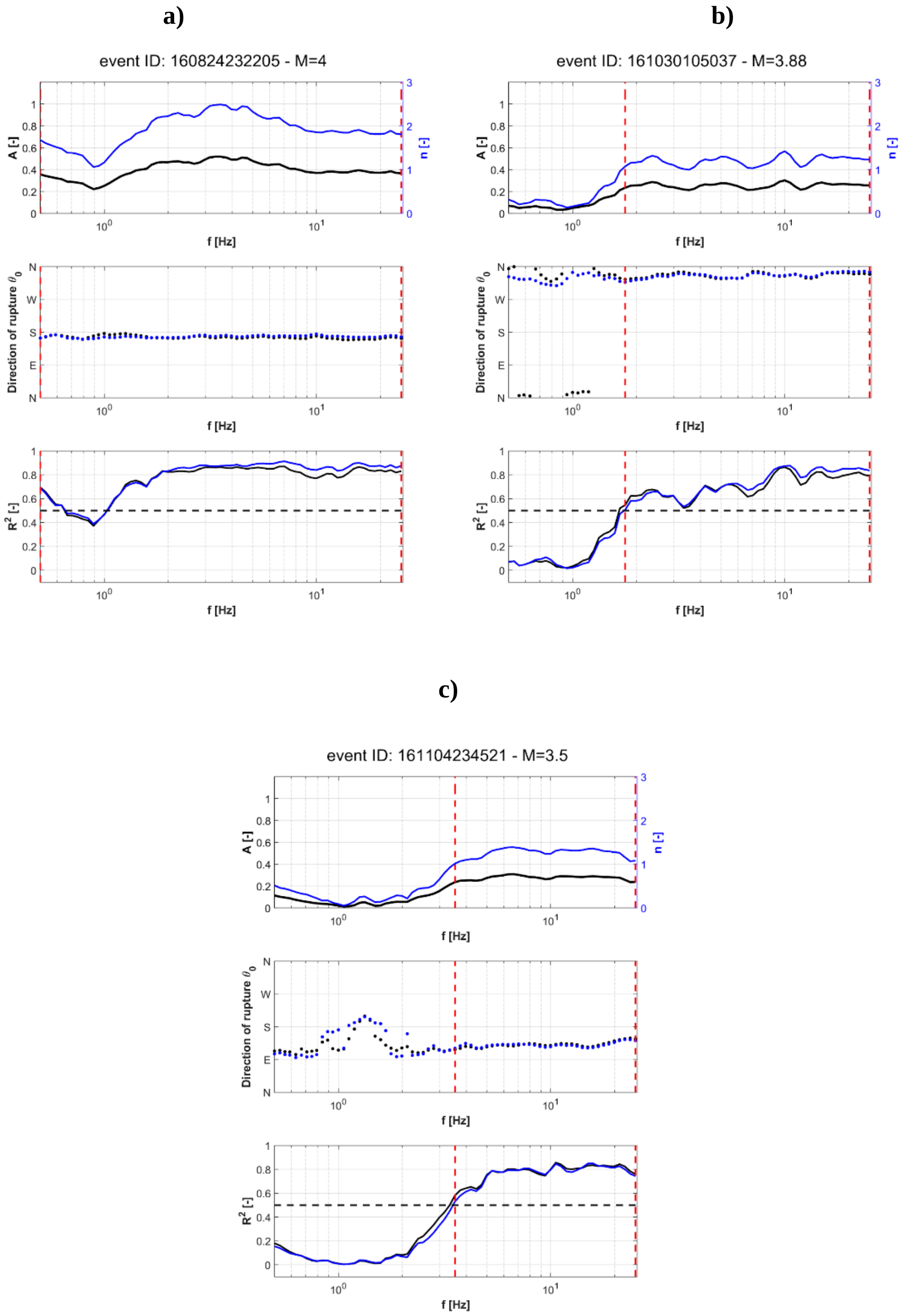

Figure S5. Amplitude (top), azimuth (middle) and regression coefficient (bottom) as a function of frequency. The black and blue curves represent fitted cosine and C_d models, respectively. Red lines represent the minimum and maximum frequency where $R^2 > 0.5$.
a) M3.4 of 24 August 2016 at 23:22:05; **b)** M3.88 of 30 October 2016 at 10:50:37; **c)** M3.5 of 04 November 2016 at 23:45:21.

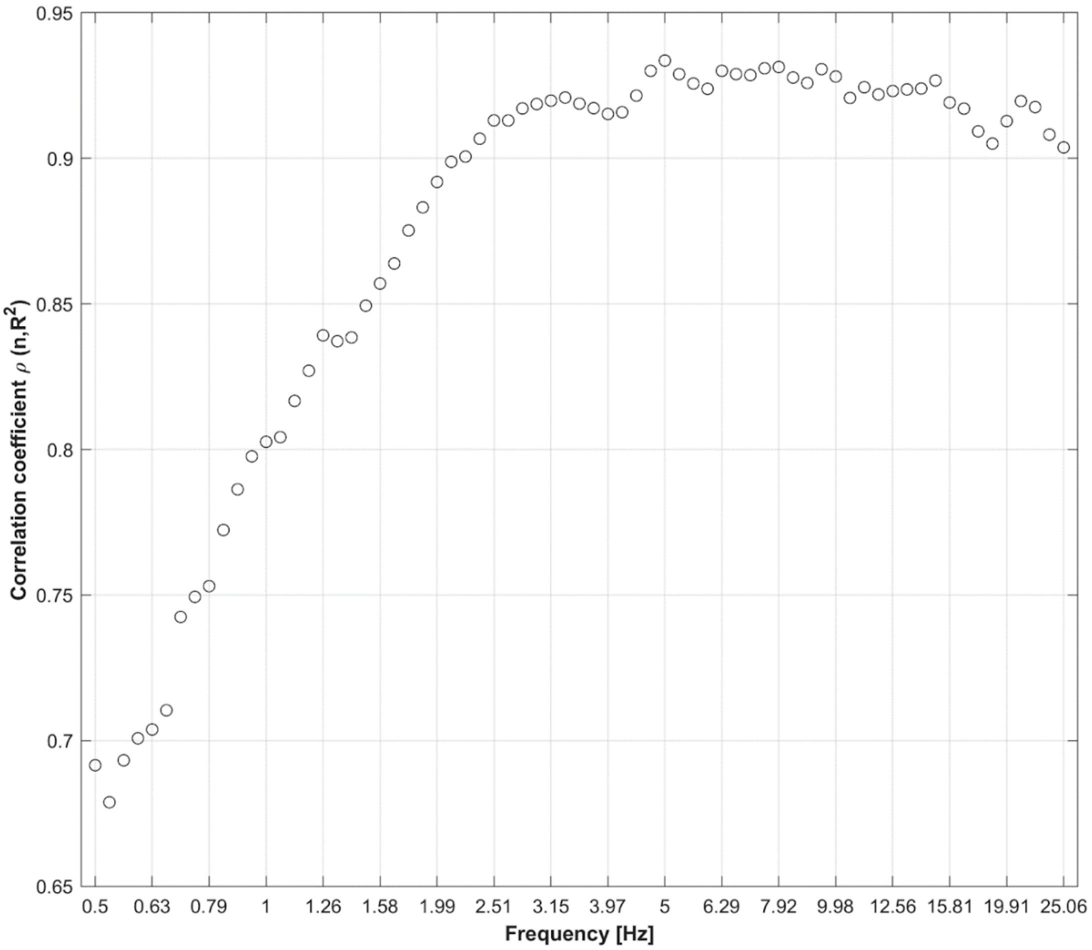

Figure S$_6$. Correlation coefficient ρ between the exponent n for the C_d model and the coefficient of determination R^2 mediated on all events.

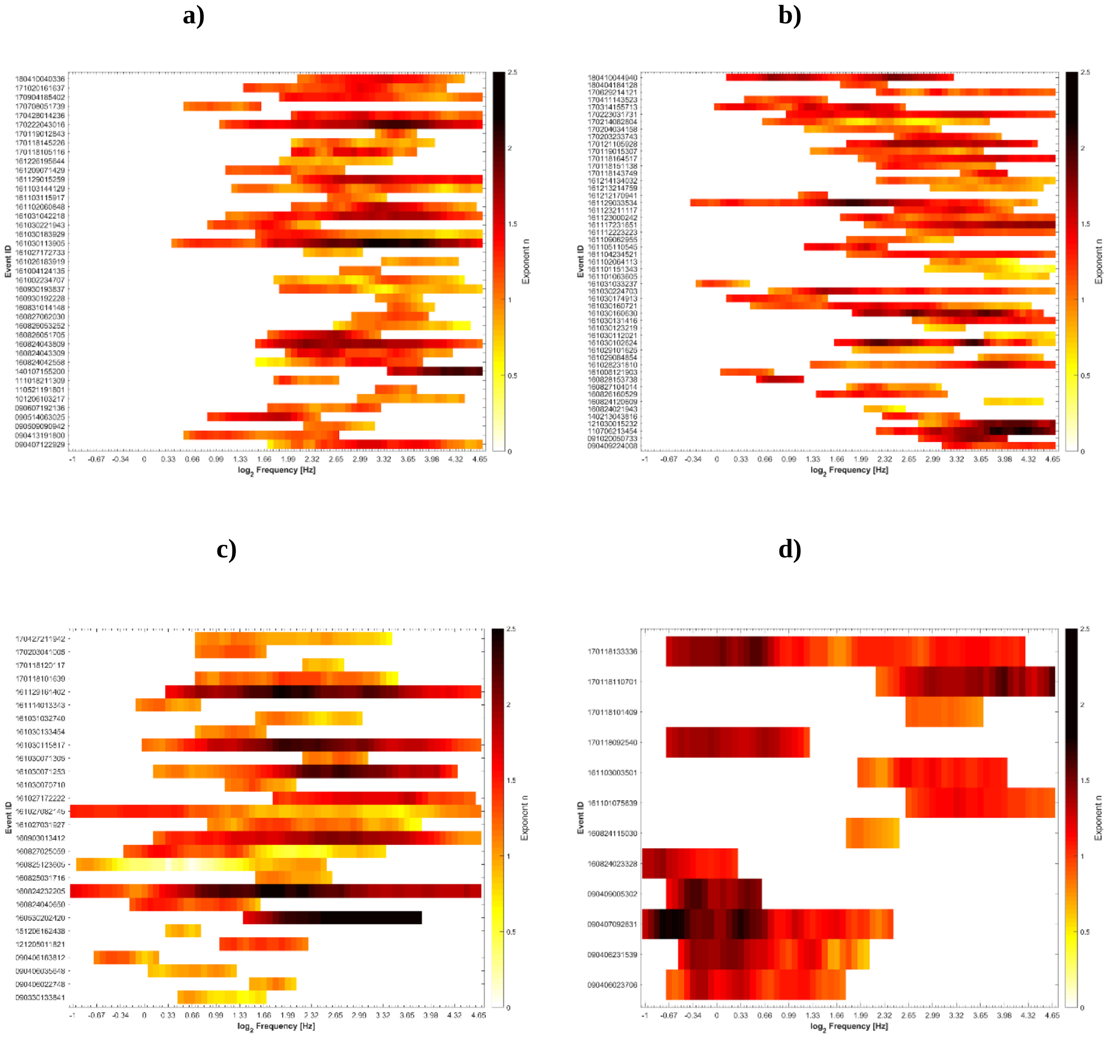

Figure S7. Amplitude, proportional to the value of the exponent n for the C_d model for each directive event as a function of frequency, divided into the following magnitude ranges: **a)** M < 3.5; **b)** 3.5 < M < 3.7; **c)** 4.0 < M < 4.5; **d)** M > 4.5.

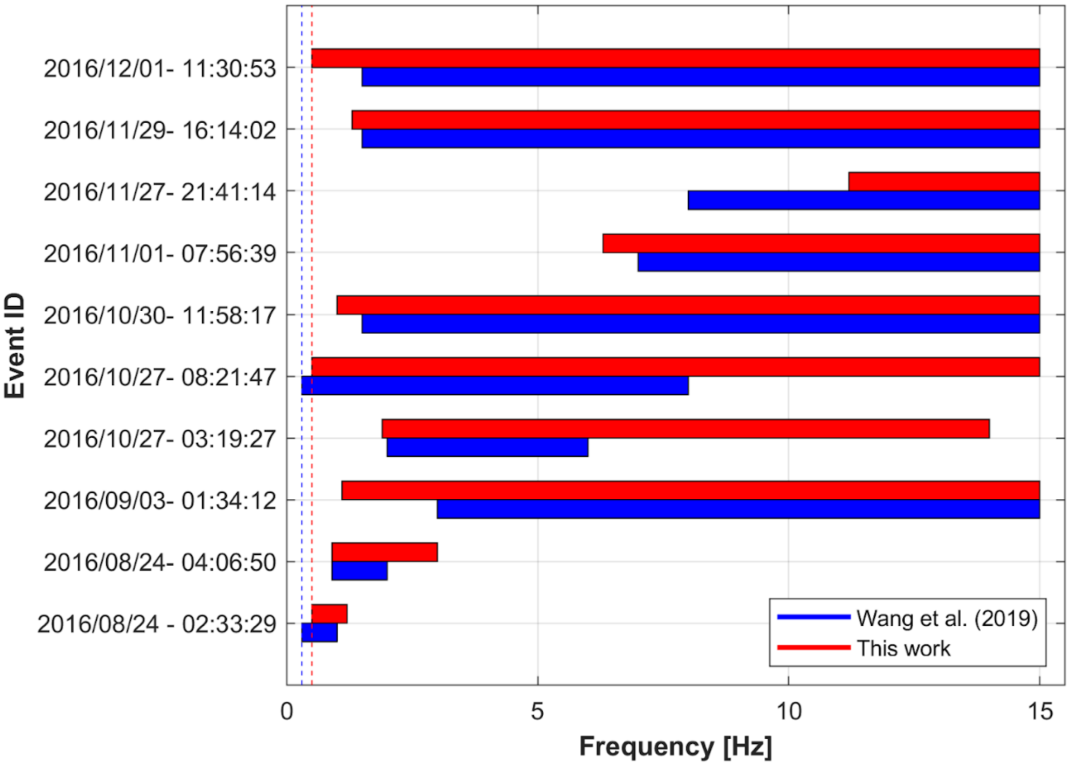

Figure S$_8$. Directivity frequency band for the 10 most directive events according to the paper of Wang et al., 2019. The blue horizontal bar marks the frequency range where the events are directive according to Wang et al., 2019, while the red horizontal bar shows the frequencies for which the event is directive in this work. Blue and red dashed lines represent respectively the lower limit to which the analysis was carried out, which is f=0.3 Hz in Wang et al. (2019) and f=0.5 Hz in this investigation.

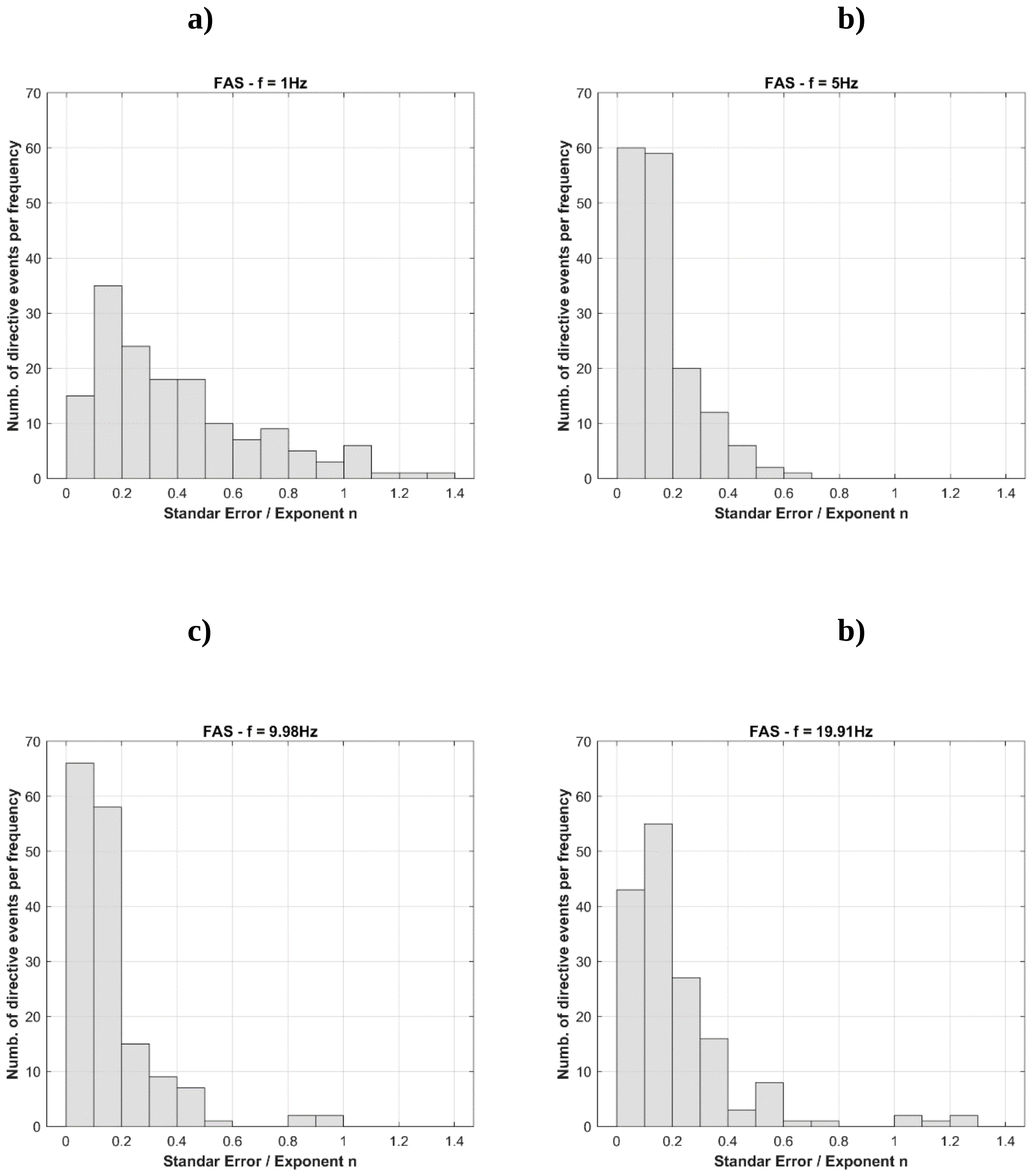

Figure S$_9$. Distribution of the ratio standard error / exponent n for 1 Hz **a)**, 5 Hz **b)**, 10 Hz **c)** and 20 Hz **d)**.

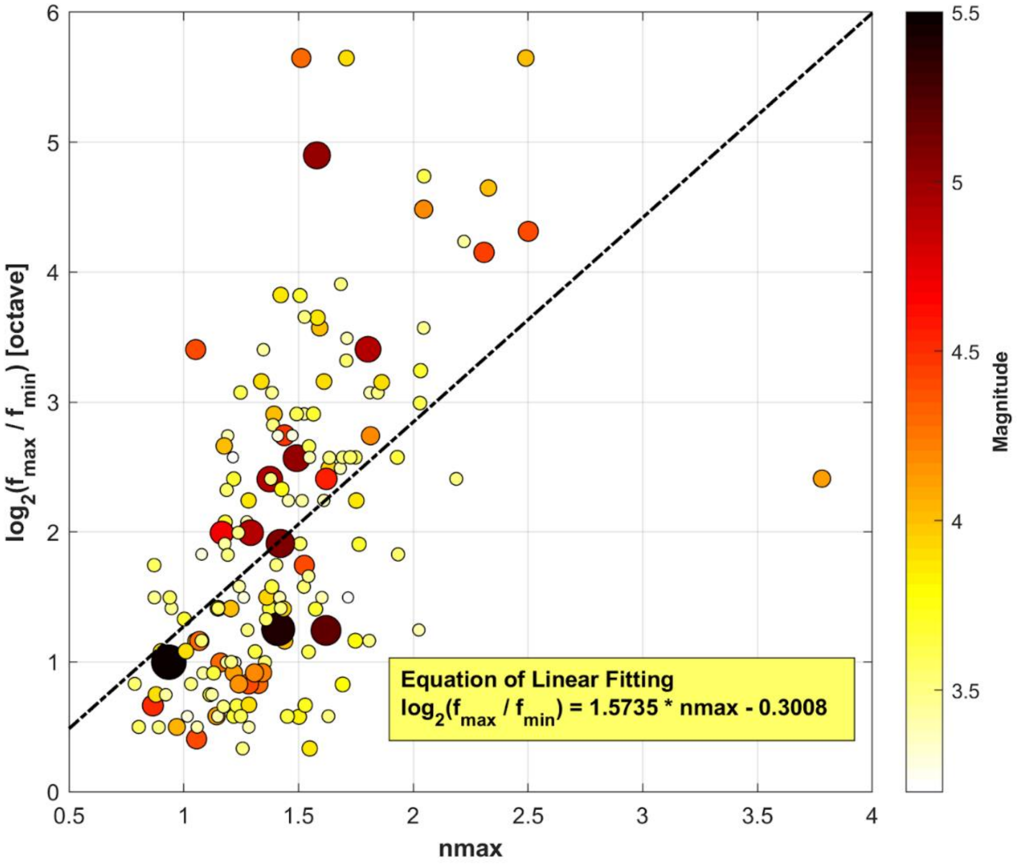

Figure S$_{10}$. Frequency bandwidth against values n_{max}. The size and color of the circles depend on magnitude; black dashed line represent the fitted curve. The yellow box shows the empirical linear relation between the frequency bandwidth and n_{max}. The correlation coefficient r between n_{max} and frequency bandwidth is 0.5195.